Nanoscale
Advances

PAPER

View Article Online
View Journal | View Issue

Cite this: *Nanoscale Adv.*, 2026, **8**, 2584

BSA-modified g-C_3N_4 nanosheets as a sustainable dual-purpose adsorbent for efficient Pb^{2+} removal and CO_2 capture

Bitupan Mohan,[ab] Rahul Sonkar,[ab] Sakyabmani Bharali[a]
and Devasish Chowdhury*[ab]

The development of high-efficiency, selective, and regenerable adsorbents for simultaneous remediation of toxic heavy metals and greenhouse gases remains a growing challenge. This work reports the synthesis of a biofunctionalized graphitic carbon nitride composite (BSA-CN) through stepwise oxidation, epoxide activation, and covalent immobilization of bovine serum albumin (BSA) onto 2D g-C_3N_4 nanosheets. Comprehensive structural, chemical, and morphological analyses (FTIR, XRD, TGA, Raman, SEM-EDX, TEM, and BET) confirmed successful protein immobilization, enhanced surface roughness, increased porosity, and the introduction of protein-derived functional groups that significantly improve surface reactivity and adsorption capacity. The BSA-CN composite exhibited exceptional adsorption performance toward Pb^{2+} ions, achieving a high monolayer capacity (292.9 mg g^{-1}), rapid uptake within 30–60 min, and strong pH-dependent interactions governed by surface charge modulation. Kinetic modeling indicates that adsorption follows a mixed physicochemical adsorption process dominated by surface complexation, best described by the pseudo-second-order and Elovich models, while equilibrium behavior fits the Redlich–Peterson and Freundlich isotherms, indicating heterogeneity and multilayer sorption. Thermodynamic analysis revealed a spontaneous and endothermic adsorption process ($\Delta G° < 0$, $\Delta H° = +45.03$ kJ mol^{-1}), accompanied by increased interfacial entropy. The composite demonstrated excellent selectivity for Pb^{2+} over Cu^{2+}, Cd^{2+} and Mn^{2+} and retained over 70% efficiency after five regeneration cycles, confirming strong operational durability. In addition, it was able to remove Pb^{2+} from real samples (lake water and surface water). Additionally, BSA-CN displayed measurable CO_2 adsorption capacity that increased at lower temperatures, attributed to enhanced interactions with its hierarchical porous architecture. Overall, this study highlights the potential of protein-functionalized g-C_3N_4 as a versatile, bio-derived, and dual-functional adsorbent for integrated heavy-metal remediation and low-temperature CO_2 capture.

Received 27th December 2025
Accepted 3rd March 2026

DOI: 10.1039/d5na01167a

rsc.li/nanoscale-advances

1. Introduction

The rapid rise in global industrialization and population growth has intensified the release of toxic heavy metals and greenhouse gases into the environment, posing severe threats to human health and ecological stability. Since the industrial revolution, CO_2 emission levels have risen by nearly 50%, reaching approximately 420 ppm, further amplifying global warming and associated environmental disruptions.[1] Unlike organic pollutants, heavy metals are non-biodegradable, persistent, and prone to bioaccumulation in living organisms.[2] They can enter the food chain, accumulate in vital organs, and cause long-term damage, even at trace concentrations. Among various toxic metals, lead (Pb^{2+}) is of particular concern due to its widespread industrial use and high toxicity.[2,3] Lead exposure is linked to severe health disorders including neurotoxicity, kidney damage, hypertension, anemia, and developmental problems in children, making its removal from aqueous systems a global priority.[3–5] The World Health Organization (WHO) has set the maximum permissible limit of Pb^{2+} in drinking water at 0.05 mg L^{-1}, underscoring the need for effective and selective remediation strategies.[5] At the same time, excess atmospheric CO_2 continues to accelerate climate change, indirectly aggravating soil and water contamination through acidification and mobilization of toxic metals.[1,6] These interlinked environmental crises highlight the critical need for innovative, sustainable, and multifunctional materials capable of addressing both heavy-metal pollution and CO_2-related environmental degradation.

Various advanced treatment methods have been applied to eliminate toxic metal ions from water including chemical

---

[a] *Material Nanochemistry Laboratory, Physical Sciences Division, Institute of Advanced Study in Science and Technology, Paschim Boragon, Garchuk, Guwahati-781035, Assam, India. E-mail: devasish@iasst.gov.in; Fax: +91 361 2279909; Tel: +91 361 2912073*

[b] *Academy of Scientific and Innovative Research (AcSIR), Ghaziabad-201002, India*

precipitation, coagulation–flocculation, ion exchange, electrochemical oxidation, advanced oxidation process, membrane filtration, photocatalysis and adsorption.[7–11] Although these techniques can achieve high removal efficiencies, they often suffer from several intrinsic limitations. Ion exchange resins, for instance, provide good selectivity but are expensive and sensitive to solution chemistry.[12] Membrane-based processes achieve high removal efficiency but are hindered by membrane fouling and energy demands while AOP-based methods require significant operational cost and often generate secondary pollutants.[13,14] These drawbacks restrict large scale applicability. In contrast, adsorption techniques have emerged as one of the most effective methods for heavy-metal removal due to their operational simplicity, cost-effectiveness, high removal efficiency, potential for adsorbent regeneration and ability to work across a wide concentration range.[15–17] The performance of adsorption processes largely depends on the physicochemical properties of the adsorbent, particularly its surface area, active functional groups and structural stability.[18] So far, a large number of adsorbents such as activated carbon, metal oxides, clays, and biochar have demonstrated considerable success.[15,19–22] However, their limited selectivity, low surface charge tunability, and poor regeneration often hinder their long-term applicability. Moreover, enhancing the selective separation of Pb^{2+} is not only conducive to environmental protection but also allows the recovery of lead metal.[23] These shortcomings highlight the urgent need for next-generation functional materials engineered with tailored binding sites, abundant heteroatoms, and strong chemical affinity to Pb^{2+}.

In recent years, two-dimensional (2D) nanomaterials such as graphene oxide, transition metal dichalcogenides (TMDs) and metal–organic frameworks (MOFs) have been widely investigated.[24–27] Despite their potential adsorption capacities, many of these materials involve complex synthesis routes, high production costs, and poor chemical stability under harsh conditions. In this context, graphitic carbon nitride (g-C_3N_4), a metal-free and nitrogen-rich polymeric semiconductor, has recently drawn significant research attention in the fields of photocatalysis, energy conversion and environmental remediation due to its nitrogen rich backbone.[28–32] Its intrinsic advantages include low-cost synthesis from abundant nitrogen rich precursors, excellent chemical and thermal stability and structural tunability.[33] Compared to other advanced nanomaterials, g-C_3N_4 offers superior stability, low toxicity risk and scalable preparation, making it suitable for sustainable water treatment applications. However, pristine g-C_3N_4 suffers from limited accessible active sites, moderate surface area, and strong interlayer stacking restricting its adsorption capacity. Various modification approaches have been reported to enhance the adsorption performance of g-C_3N_4, such as thermal exfoliation, heteroatoms doping, introducing oxygen-containing groups, and surface functionalization.[30,34,35] Oxidation of g-C_3N_4 can produce hydroxyl and carboxyl functionalities on its surface, thereby increasing hydrophilicity and metal-binding ability.[35,36] Further functionalization of pre-carboxylated or oxidized g-C_3N_4 surfaces introduces new chemical moieties on its surface *via* amide linkage or epoxidation reactions.[35,37,38] Among different functional strategies biofunctionalization using biomolecules offers unique advantages because biological macromolecules inherently possess diverse functional groups capable of strong, selective bindings with metal ions.[35,39,40]

Biomolecules such as bovine serum albumin (BSA), collagen, casein, or engineered peptides offers a rich distribution of amine (–NH_2), carboxyl (–COOH), hydroxyl (–OH) and thiol (–SH) functional groups, which can strongly interact with metal ions through complexation, electrostatic attraction, and coordination bonding.[40–42] Importantly, proteins may also contribute to enhanced hydrophilicity, increased surface heterogeneity, and improved biocompatibility of the adsorbent. Bovine serum albumin (BSA), in particular, is an inexpensive, stable, and readily available protein with a molecular structure rich in amino acid residues that can act as active sites for metal adsorption.[42] Its three-dimensional conformation provides a variety of binding domains, enabling selective interaction with soft and borderline Lewis's acids such as Pb^{2+}. The immobilization of BSA onto nanomaterials can therefore significantly enhance their adsorption capacity and selectivity.[44,45] In addition to metal binding, proteins also exhibit notable potential for CO_2 adsorption. In biological systems, proteins such as hemoglobin naturally bind and transport CO_2, forming carbamino complexes, demonstrating the inherent ability of amino groups to react with CO_2.[46] Beyond biological systems, emerging studies show that solid-state proteins are also capable of interacting with CO_2, indicating their promise as bio-based sorbents.[47] For instant, Mitsuda *et al.* showed that solid proteins including casein, raw silk, and gelatin can adsorb significant amounts of CO_2 with high selectivity compared to other gases.[46] Although several studies have modified g-C_3N_4 with inorganic dopants or polymers, protein-based functionalization remains largely unexplored, especially regarding how protein–polymer interactions modify surface chemistry, charge distribution, and their mechanistic effect on Pb^{2+} uptake and performance under varying environmental conditions (pH, dosage, temperature, and competing ions). Additionally, few reports address the broader implications of such materials in relation to CO_2-driven environmental challenges or evaluate their regeneration potential over repeated use. Therefore, understanding how such biomolecular functionalization influences adsorption kinetics, isotherm behavior, and thermodynamic feasibility is essential for designing materials suited for real wastewater systems.

This study aims to develop a BSA biofunctionalized g-C_3N_4 composite (BSA-CN) adsorbent for efficient and selective adsorption of Pb^{2+} from aqueous systems. The work focuses on controlled oxidation and epoxy mediated protein immobilization onto exfoliated g-C_3N_4, thereby introducing abundant amino, carboxyl, and peptide coordination sites for enhanced metal binding. Comprehensive physicochemical characterization, including FTIR, XRD, Raman spectroscopy, TGA, TEM, SEM-EDX, BET surface area analysis and zeta potential measurements was performed to confirm successful structural modification and to elucidate changes in functional groups, morphology, surface area and charge distribution. Adsorption performance was systematically evaluated under varying pH, concentration, temperature, and contact time conditions, while the mechanism was elucidated using non-linear kinetic and isotherm modeling supported by thermodynamic analysis. Beyond its aqueous metal remediation, the protein modified g-C_3N_4 also demonstrates significant CO_2 adsorption at low pressure, highlight its viability as a dual-function materials for environmental remediation.

2. Materials and methods

2.1. Materials

Sodium hydroxide pellets (NaOH), nitric acid (HNO_3, 69%), potassium permanganate ($KMnO_4$), hydrogen peroxide (H_2O_2, 30%) and melamine (99%) were obtained from Merck Life Science Pvt. Ltd. Hydrochloric acid (6 N aqueous solution), urea (AR, 99.5%), phosphate-buffered saline (PBS, pH of 7.4 ± 0.1) and epichlorohydrin (AR, 99.5%) were purchased from Sisco Research Laboratory Pvt. Ltd. Bovine serum albumin (BSA) was obtained from HiMedia Laboratories Pvt. Ltd. Standard solutions of heavy-metal salts including $Mn(NO_3)_2 \cdot 4H_2O$, $Zn(NO_3)_2$ and $Cu(NO_3)_2 \cdot 3H_2O$ were purchased from Merck and $Pb(NO_3)_2$ and $Cd(NO_3)_2 \cdot 3H_2O$ were also purchased from Sisco Research Laboratory Pvt. Ltd and used without further purification. All chemicals were of analytical grade, and deionized water was used throughout the experiments.

2.2. Synthesis and oxidation of g-C_3N_4

The synthesis of g-C_3N_4 was conducted *via* the thermal polymerization of urea and melamine as shown in Fig. 1. In a standard synthesis procedure, 6 grams of urea and 4 grams of melamine were mixed in a mortar and pestle to yield g-C_3N_4 in a single reaction vessel. The resultant powder was subsequently transferred into a covered crucible and subjected to heating in a muffle furnace at a temperature of 550 °C for a duration of 4 hours. Upon completion of the heating phase, the furnace was permitted to cool down to ambient temperature. The resultant powder sample manifested a pale-yellow tint.

The synthesized g-C_3N_4 was oxidized by using a previously reported method.[25] In this technique, 1 g of g-C_3N_4 powder was combined with 30 mL of HNO_3 in a single-neck flask and stirred magnetically for 30 minutes. After progressively adding 3.5 g of $KMnO_4$ to the flask, the mixture was kept in an ice bath and vigorously stirred for 2 hours. The mixture was blended with 90 mL of deionized water and ultrasonically treated for 2 hours. The mixture was then stirred at room temperature for another 8 hours. To neutralize leftover $KMnO_4$, 20 mL of a 30% hydrogen peroxide (H_2O_2) solution was carefully added. The white product was separated by centrifugation at 6000 rpm and washed with DI water until the pH was approximately neutral. Finally, the oxidized g-C_3N_4 (Ox-CN) nanosheets were produced as a white powder.

2.3. Surface functionalization *via* epoxide–amine coupling

To immobilize protein moieties onto the surface of hydroxylated 2D g-C_3N_4, a two-step functionalization strategy involving epoxidation of surface –OH groups followed by epoxy–amine coupling was employed (Fig. 1). Initially, 200 mg of the hydroxyl-functionalized g-C_3N_4 (Ox-CN) was dispersed in a 1 : 1 (v/v)

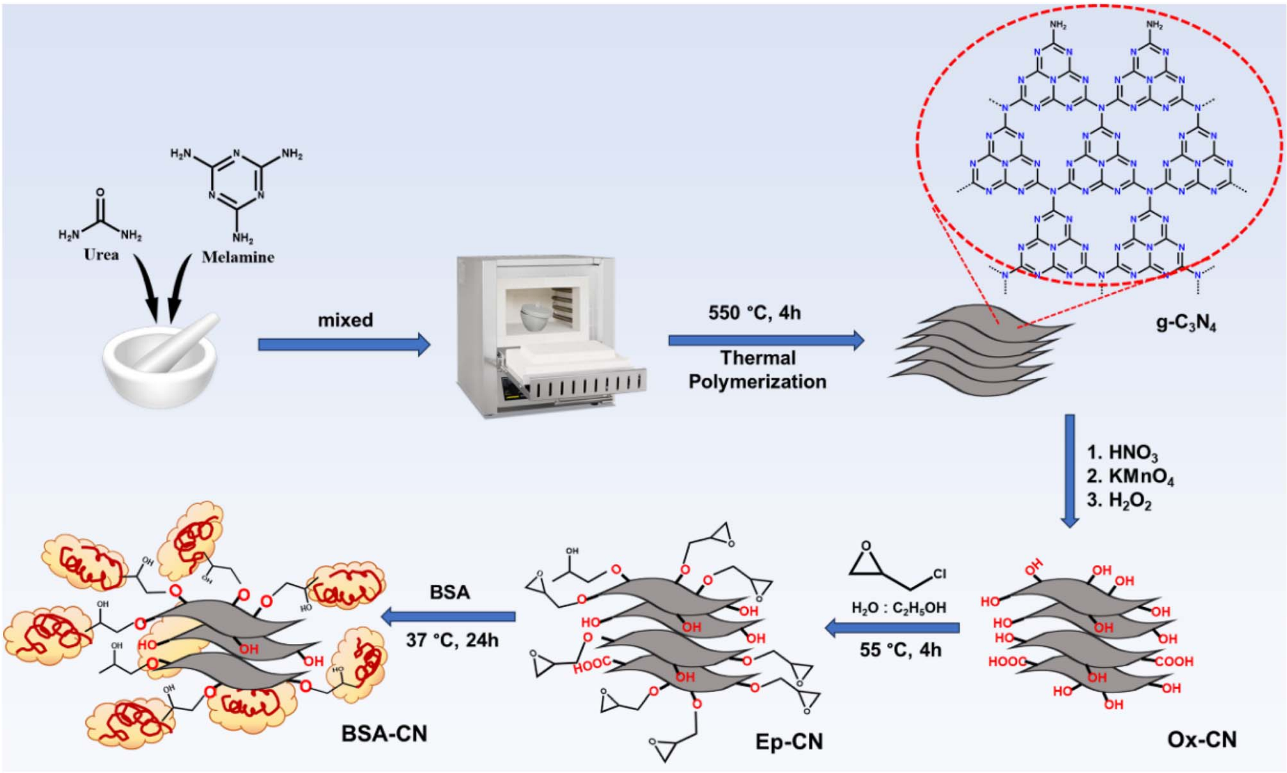

Fig. 1 Overall reaction scheme of protein functionalized g-C_3N_4.

ethanol–deionized water mixture (40 mL) using ultrasonication for 30 min to ensure uniform dispersion. The pH of the suspension was adjusted to ∼9–10 by adding 0.1 M NaOH dropwise under continuous stirring. Subsequently, 2 mL of epichlorohydrin was added dropwise to the alkaline suspension under a nitrogen atmosphere, and the reaction mixture was stirred at 50 °C for 8 h. Upon completion, the mixture was cooled to room temperature and neutralized using dilute HCl (0.1 M). The product was separated by centrifugation (6000 rpm, 10 min), washed thoroughly with ethanol and deionized water to remove unreacted epichlorohydrin, and finally freeze-dried to obtain the epoxide-functionalized nanomaterial (designated as Ep-CN).

For covalent immobilization, 100 mg of Ep-CN was redispersed in 25 mL of phosphate buffer (0.05 M, pH 8.5) containing the target protein BSA (100 mg). The reaction mixture was stirred at 37 °C for 24 h to facilitate nucleophilic attack of the primary amine group on the epoxy moieties, leading to ring opening and covalent bonding. The resulting biofunctionalized nanomaterial was collected by centrifugation, washed multiple times with deionized water to remove unbound residues, and dried under vacuum at 40 °C. The final product was designated as BSA-CN.

2.4. Characterization and measurements

The synthesized nanomaterials and adsorbent were characterized using various analytical techniques. Fourier Transform Infrared (FTIR) spectroscopy was carried out in ATR mode by using a PerkinElmer Spectrum Two FTIR instrument. X-ray diffraction (XRD) analysis was conducted using a Bruker D8 Advance X-ray diffractometer (Karlsruhe, Germany) with Cu Kα radiation ($\lambda = 1.54056$ Å) at a scan rate of 1.5 s per step over an angular range of $2\theta = 5$–80°. The operating conditions of the XRD tube were maintained at 40 mA and 40 kV. Thermogravimetric analysis (TGA) was performed using a PerkinElmer4000 instrument for all thermal analyses of samples. Raman analysis was carried out using a Micro Raman spectrometer (Lab RAMUV VIS-NIR, Horiba). Investigation of surface charge and zeta potential was performed at room temperature using a zeta potential analyzer (Malvern-NanoZS90). Transmission electron microscopy (TEM) was carried out with a JEOL TEM-2100 instrument (Tokyo, Japan) to examine the morphology and SAED pattern of the prepared composite. The surface morphology and elemental composition of the nanomaterials and composite films were investigated using a SIGMA VP (ZEISS) scanning electron microscope (SEM) (Oberkochen, Germany) equipped with an energy-dispersive X-ray (EDX) spectroscopy unit. The specific surface area of CN and the adsorbent composite were obtained from N_2 adsorption–desorption isotherms by employing the Brunauer–Emmett–Teller (BET) method (Quantachrome iQ autosorb analyzer, USA) and the mean pore size was measured with the help of the Barrett–Joyner–Halenda (BJH) approach.

2.5. Adsorption experiments

Batch adsorption experiments were conducted to evaluate the influence of key operational variables, including initial pH, temperature, adsorbent dosage, and initial Pb^{2+} concentration, on the adsorption performance of the synthesized BSA-CN composite. A stock solution of Pb^{2+}, Cd^{2+}, Cu^{2+}, Zn^{2+}, and Mn^{2+} with a concentration of 1000 mg L^{-1} was prepared by dissolving $Pb(NO_3)_2$, $Mn(NO_3)_2\cdot 4H_2O$, $Cu(NO_3)_2\cdot 3H_2O$, $Cd(NO_3)_2\cdot 3H_2O$ and $Zn(NO_3)_2$ in deionized water. Working solutions of desired concentrations (10–70 mg L^{-1}) were obtained by appropriate dilution with DI water. For each experiment, a known mass of adsorbent (10–40 mg) was dispersed in 50 mL of Pb^{2+} solution in 100 mL capacity conical flasks. The flasks were agitated at 180 rpm in an orbital shaker at predetermined temperatures (25–55 °C) for 10–240 min to attain equilibrium. The initial pH of the Pb^{2+} solution was adjusted between 2 and 10 using 0.1 M HCl or 0.1 M NaOH. Based on preliminary pH screening, maximum adsorption was observed near pH 6–8; therefore, subsequent studies on kinetics, isotherms, and thermodynamic parameters were conducted at neutral pH. After the contact period, the suspensions were filtered to separate the adsorbent. The residual concentration of the filtrate was determined using Atomic Absorption Spectroscopy (AAS, Model ICF3300 Themo Fisher Scientific).

The adsorption capacity (Q_t, mg g^{-1}) and percentage removal (R%) were calculated using the following equations:

$$Q_t = \frac{(C_o - C_t)}{m} \times V \tag{1}$$

$$\%R = \frac{(C_o - C_t)}{C_o} \times 100 \tag{2}$$

where C_o and C_e are the initial and equilibrium concentrations (mg L^{-1}), respectively, V is the solution volume (L), and m is the adsorbent mass (g). All experiments were carried out in triplicate, and the mean values are reported.

2.6. Kinetic and isotherm model studies

Kinetic experiments were carried out using 0.2 g L^{-1} of BSA-CN in 50 mL of Pb^{2+} solution (30 mg L^{-1}) at pH 7. Samples were withdrawn at selected time intervals (10–240 min), and the concentration of Pb^{2+} was measured as described above. The kinetic data were fitted to the pseudo first order (PFO), pseudo second order (PSO) and Elovich kinetic models which are expressed as follows

$$Q_t = Q_e(1 - e^{-k_1 t}) \tag{3}$$

$$Q_t = \frac{{Q_e}^2 k_2 t}{1 + Q_e k_2 t} \tag{4}$$

$$Q_t = \frac{1}{\beta}\ln(1 + \alpha\beta t) \tag{5}$$

where Q_t and Q_e (mg g^{-1}) represent the adsorption capacity at time t and at equilibrium, respectively, k_1 (min^{-1}) is the PFO rate constant, and k_2 (g mg^{-1} min^{-1}) is the PSO rate constant, α (mg g^{-1} min^{-1}) the initial adsorption rate, and β (g mg^{-1}) the desorption-related constant. Model parameters were determined by non-linear regression.

Equilibrium isotherm experiments were conducted by varying the initial Pb^{2+} concentration (10–70 mg L^{-1}), while maintaining the adsorbent dosage at 0.2 g L^{-1} and pH at 7. The suspensions were agitated for 180 min to reach equilibrium. After equilibration, the adsorption data were fitted using four non-linear isotherm models: Langmuir, Freundlich, Temkin, and Redlich–Peterson (R–P) models which are expressed as follows:

$$Q_e = \frac{Q_m K_L C_e}{1 + K_L C_e} \tag{6}$$

where Q_m (mg g^{-1}) is the maximum monolayer capacity and K_L (L mg^{-1}) is the Langmuir constant.

$$Q_e = K_F {C_e}^{1/n} \tag{7}$$

where K_F represents the adsorption capacity and n denotes the adsorption intensity

$$Q_e = B \ln(K_T C_e) \tag{8}$$

$$B = \frac{RT}{b}$$

where, B (J mol^{-1}) relates to the heat of adsorption, K_T (L g^{-1}) is the Temkin binding constant, and b (J mol^{-1}) indicates the interaction between the adsorbent and adsorbate.

$$Q_e = \frac{K_R C_e}{1 + a_R {C_e}^{\beta}} \tag{9}$$

where K_R (L g^{-1}) and a_R (L mg^{-1}) are adsorption constants, and β ($0 \leq \beta \leq 1$) indicates the system's deviation between Langmuir ($\beta = 1$) and Freundlich ($\beta = 0$) behavior.

All isotherm parameters were estimated using non-linear curve fitting to minimize error and avoid distortions associated with linear transformations.

2.7. Thermodynamic studies

Thermodynamic parameters were obtained by performing equilibrium adsorption at different temperatures (298, 308, 318, and 328 K). The thermodynamic equilibrium constant (K_{ad}) was calculated from the ratio of adsorbed to solution-phase Pb^{2+} concentration, and plotted using the van't Hoff equation:

$$\ln K_{ad} = -\frac{\Delta H^\circ}{RT} + \frac{\Delta S^\circ}{R} \tag{10}$$

The Gibbs free energy change was calculated using

$$\Delta G^\circ = \Delta H^\circ - T\Delta S^\circ \tag{11}$$

The activation energy of the adsorption process was calculated by using the Arrhenius equation as follows

$$\ln k = \ln A - \frac{E_a}{RT} \tag{12}$$

where k is the rate from the PSO kinetic equation at different temperatures (298 K, 308 K and 318 K), A is the pre-exponential factor, E_a is the activation energy (kJ mol^{-1}), R is the universal gas constant (8.314 J mol^{-1} K^{-1}), and T is the temperature (K).

2.8. Adsorbent reusability

From an economic perspective, regeneration of the adsorbent is crucial for practical applications. The adsorbent can be utilized again by desorbing the adsorbed Pb^{2+} once adsorption equilibrium has been reached. The reusability tests were carried out by subjecting Pb^{2+} loaded BSA-CN to repeated adsorption–desorption cycles under identical operating conditions. After completing each adsorption experiment, the Pb^{2+} loaded adsorbent was transferred to 50 mL of 0.1 M HCl solution and shaken for 45 min at 180 rpm to promote desorption. Hydrochloric acid was selected as the regenerating agent due to its to its strong acidic nature, high solubility of lead chloride complexes, minimal structural degradation of the protein-functionalized nanosheets, low cost, and easy availability. Following desorption, the suspension was centrifuged, and the desorbed Pb^{2+} concentration was determined by atomic absorption spectrophotometry (AAS) to quantify the amount of metal released. The regenerated adsorbent was thoroughly rinsed with deionized water until neutral pH, dried at 40 °C, and reused for the next adsorption cycle under the same conditions as the initial run. The desorption efficiency was calculated using the following equation:

$$\text{Desorption efficiency}(\%) = \frac{\text{Amount of Pb(II)desorbed}}{\text{Amount of Pb(II)adsorbed}} \times 100 \tag{13}$$

2.9. CO_2 adsorption set-up

CO_2 adsorption experiments were conducted using a gas sorption analyzer. Measured amounts of BSA-CN were degassed at a controlled temperature with helium serving as the carrier gas. Using an external water bath, the sample was set to the desired temperatures (25, 13, and 3 °C), and the CO_2 flow was regulated by the gas sorption analyzer. The pressure was maintained between 0.05 and 0.99 atm., and the CO_2 adsorption isotherm was subsequently measured.

3. Results and discussion

3.1. Structural and morphological characterization of the adsorbent

First, the stepwise functionalization of g-C_3N_4 was confirmed through FTIR spectroscopy and are shown in Fig. 2(a). The pristine g-C_3N_4 (CN) spectrum displayed the characteristic features of the heptazine framework, including multiple intense absorption bands within the 1200–1650 cm^{-1} region, which are assigned to the stretching vibrations of C–N and C=N heterocycles. Additionally, a prominent peak was observed at 811 cm^{-1}, attributed to the out-of-plane bending vibration of the *s*-triazine units. A broad absorption band centered at 3100–3300 cm^{-1} was also observed, resulting from terminal –NH_2 and –OH groups as well as adsorbed water, which is consistent with previous reports on polymeric carbon nitride.[30,36] Following

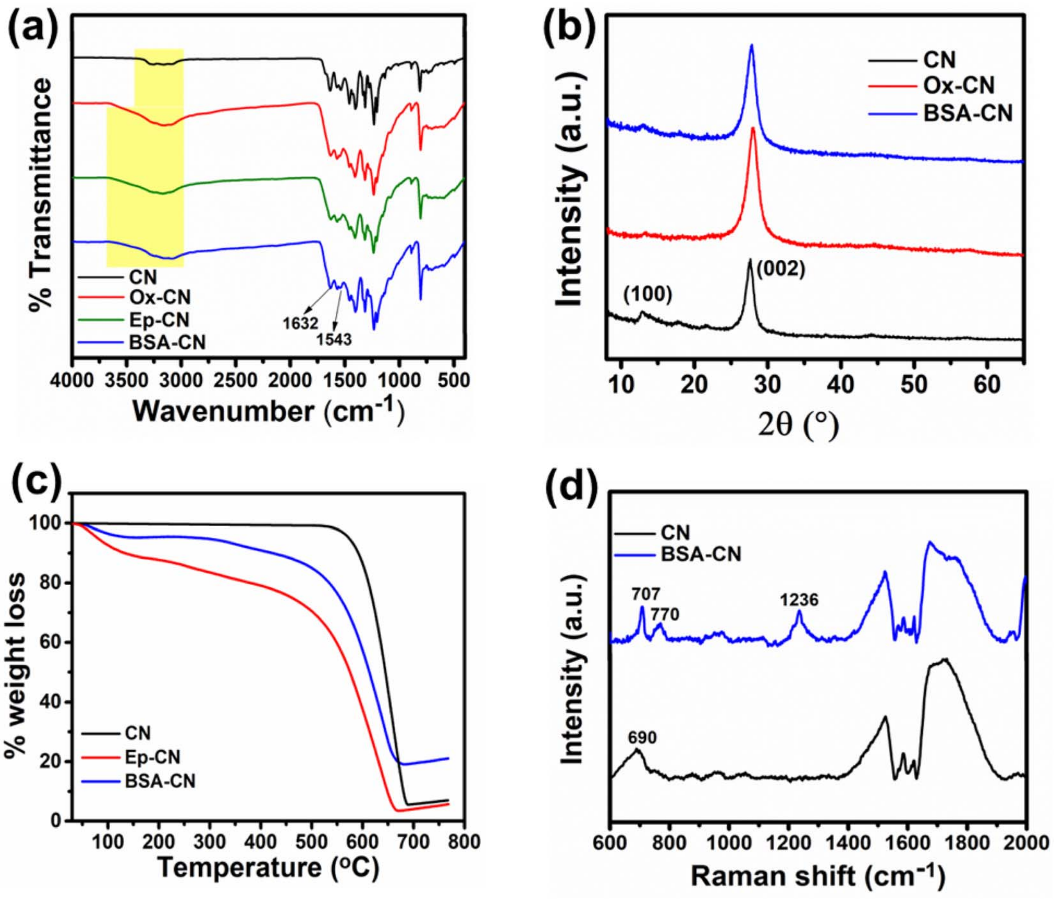

Fig. 2 Physicochemical characterization of the synthesized BSA composite. (a) FTIR spectra of CN, Ox-CN, Ep-CN and BSA-CN, (b) XRD plot of CN, Ox-CN and BSA-CN, (c) TGA plots of CN, Ep-CN and BSA-CN in a N_2 environment, and (d) Raman plot of CN and BSA-CN recorded using a 633 nm laser.

nitric acid–$KMnO_4$ oxidation (Ox-CN), significant spectral changes were observed. A new broad band in the 3050–3500 cm^{-1} region appeared, corresponding to the stretching vibrations of –OH groups introduced during oxidation, confirming successful incorporation of oxygenated groups.[36] After epichlorohydrin-treatment (Ep-CN), the characteristic oxirane bands expected around 910–925 and 840–855 cm^{-1} were not clearly resolved. This absence can be attributed the inherently weak intensity of epoxy vibrations compared to the dominant heptazine breathing band at ∼810 cm^{-1} and partial ring-opening of epoxides under aqueous alkaline conditions, which generates chlorohydrin or diol-type linkages that do not display sharp oxirane features.[48] Despite the lack of these distinct peaks, other spectral changes confirm successful surface modification. Specifically, new aliphatic C–H stretching bands appeared near 2920 cm^{-1}, the C–O stretching region (1000–1200 cm^{-1}) became more intense, and the broad O–H absorption diminished, consistent with consumption of hydroxyl groups. These features collectively indicate that epichlorohydrin was covalently grafted onto CN, producing a mixture of epoxy, and ether linkages. Importantly, such functionalities remain highly reactive toward nucleophiles such as amines, thereby enabling the subsequent conjugation of BSA to the nanosheets. Although the protein's vibrational modes partially overlap with the intrinsic framework peaks of g-C_3N_4, distinct signatures of BSA can still be discerned in the BSA-CN spectrum. The most prominent evidence comes from the amide I band (∼1632 cm^{-1}), arising from C=O stretching of peptide linkages, while a weaker feature around 1543 cm^{-1} corresponds to the amide N–H bending coupled with C–N stretching.[43] These characteristic features unambiguously confirm the successful conjugation of BSA onto the surface of the epoxide-functionalized g-C_3N_4.

The crystalline structure of the samples was investigated using X-ray diffraction (XRD), and the results are shown in Fig. 2(b). The pristine g-C_3N_4 exhibited two characteristic reflections at $2\theta \approx 12.9°$ and 27.7°, corresponding to the (100) in-plane structural packing of tri-*s*-triazine units and the (002) interlayer stacking of the aromatic conjugated layers, respectively (JCPD Card No. 00-066-0813). From the card number the phase of the nanomaterials was confirmed to be orthorhombic in nature. The intense peak at 27.7° indicates well-ordered stacking of the graphitic planes, while the weaker diffraction at 12.9° corresponds to the periodic arrangement of heptazine motifs.[49] Upon oxidation (Ox-CN), the (002) peak becomes broader and shifts, indicating partial disruption of the π–π stacking due to the introduction of oxygen-containing functionalities, which expand the interlayer distance.[36] The (100) diffraction at 13° was further weakened, supporting the loss of in-plane periodicity following oxidative treatment. The broadening of the peaks indicates that the crystallinity of the materials decreases. The intensity of the peaks slightly decreases compared to the pristine material, indicating a change in crystallite size. These results are consistent with FTIR evidence of oxygen-containing groups, which disrupt the ordered conjugated network. Notably, after BSA immobilization, the (002) reflection remained at 27.7°, suggesting that protein attachment occurs primarily through surface binding rather than significant intercalation between the g-C_3N_4 layers. This retention of the (002) position, together with peak broadening, supports successful BSA immobilization while maintaining the layered framework of CN. The peaks remain at the same positions, indicating that the phase of the material has not changed after modification.

Furthermore, the surface charge evolution of g-C_3N_4 during successive functionalization steps was monitored by zeta potential measurements (pH 7 ± 0.1) and is shown in Fig. S1. Pristine g-C_3N_4 exhibited a moderately negative zeta potential of -11.9 mV, arising from deprotonated edge nitrogen sites. Upon oxidative treatment (Ox-CN), the zeta potential decreased markedly to -18.2 mV, confirming the successful incorporation of oxygenated moieties (–COOH and –OH) that dissociate under neutral conditions. Subsequent activation with epichlorohydrin (Ep-CN) resulted in partial neutralization of these surface charges, reflected by a positive potential of 6 mV, as the epoxy linkers masked carboxyl/hydroxyl functionalities. Following BSA immobilization (BSA-CN), the zeta potential further decreased to -23.3 mV, consistent with the presence of BSA, which carries a net negative charge at physiological pH due to its low isoelectric point ($\sim$4.7).[50] These systematic shifts in surface charge confirm the successful stepwise modification of g-C_3N_4 and highlight the dominant contribution of protein adsorption to the final colloidal stability.

Subsequently, the thermal stability and organic content of the materials were examined by TGA under a nitrogen atmosphere as shown in Fig. 2(c). The pristine CN exhibited excellent thermal stability, showing negligible weight loss below 500 °C. The main decomposition occurred in the range of 540–700 °C, corresponding to the breakdown of the heptazine framework, leaving a small char residue of 5.5% beyond 700 °C.[51] In contrast, the epoxide-functionalized sample (Ep-CN) displayed additional weight loss between 200 and 400 °C, corresponding to the grafted epichlorohydrin moieties introduced during the process. The overall weight loss was significantly higher than that of pristine CN, confirming the successful introduction of organic linkers onto the nanosheets. The major degradation of the g-C_3N_4 backbone still occurred at $\sim$500 °C, although with a slightly lower onset temperature, indicating that surface modification reduced the thermal stability of the framework. For the protein-functionalized sample (BSA-CN), a two-step decomposition profile was observed. The initial weight loss below 150 °C was associated with the release of bound water, followed by a clear degradation stage between 200 and 400 °C, which can be ascribed to the thermal decomposition of immobilized BSA. The subsequent mass loss at 500–650 °C corresponded to the decomposition of the underlying g-C_3N_4 matrix. Compared to Ep-CN, BSA-CN exhibited intermediate thermal stability, with higher residual mass at 700 °C due to the contribution of proteinaceous carbonaceous residues.

Raman spectra of pristine CN and BSA-immobilized g-C_3N_4 (BSA-CN), collected under 633 nm excitation, are presented in Fig. 2(d). The spectrum of pristine CN exhibits a distinct band at 690 cm^{-1}, which corresponds to the characteristic breathing vibration of the tri-*s*-triazine (heptazine) units, confirming the structural integrity of the g-C_3N_4 framework.[52] Additionally, broad features between 1550 and 1700 cm^{-1} can be attributed to C–N and C═N stretching vibrations within the conjugated network. Following BSA immobilization, several new Raman-active modes emerge. Peaks at 707 and 770 cm^{-1} arise from protein-related skeletal vibrations, while the band at 1236 cm^{-1} is characteristic of amide III (C–N stretching coupled with N–H bending).[53] A strong and broad feature in the 1600–1700 cm^{-1} range is attributed to the amide-I band, arising primarily from C═O stretching of the peptide backbone. These new vibrational signatures confirm the successful immobilization of BSA on the CN surface.

The morphological changes on the surface of CN after BSA immobilization were observed by SEM and the corresponding elemental composition was confirmed through EDX analysis. SEM images of pristine CN, oxidized CN (Ox-CN), and BSA-CN are presented in Fig. 3. As illustrated in Fig. 3(a), the pristine CN displays the characteristic aggregated, layered, and crumpled nanosheet-like morphology, typical of polymeric carbon nitride obtained through thermal polymerization. The corresponding EDX spectrum (Fig. 3(a')) shows dominant signals of carbon (32.04 wt%) and nitrogen (62.19 wt%), along with a small amount of oxygen (5.77 wt%), which likely originates from surface hydroxylation or adsorbed moisture. The high nitrogen atomic percentage (59.45%) confirms the presence of tri-*s*-triazine frameworks containing abundant amine and imide nitrogen. Upon oxidative treatment, the Ox-CN sample (Fig. 3(b)) displays a more fragmented and rough morphology. The increase in structural roughness and agglomeration indicates partial oxidation, exfoliation damage, and formation of defect sites. This morphological evolution is consistent with the introduction of hydrophilic –OH and –COOH groups, as also confirmed by the increased oxygen content from 5.77 wt% to 10.11 wt%, in the EDS profile, confirming successful surface oxidation. Additionally, the AFM topographic image of Ox-CN (Fig. S2) shows well-dispersed, exfoliated sheets without severe restacking and the corresponding height profile indicates thickness variations in the range of $\sim$1.5–2.4 nm. Subsequent BSA immobilization (Fig. 3(c)) produces a further change in surface texture, with the appearance of more irregular, clustered aggregates, suggestive of protein adsorption onto the CN framework. The EDS spectrum (Fig. 3(c')) further reveals a pronounced increase in oxygen content (11.39 wt%), accompanied by the appearance of sulphur (0.31 wt%), which can be attributed to the cysteine and methionine residues in BSA. This compositional shift, together with the attenuation of the C/N

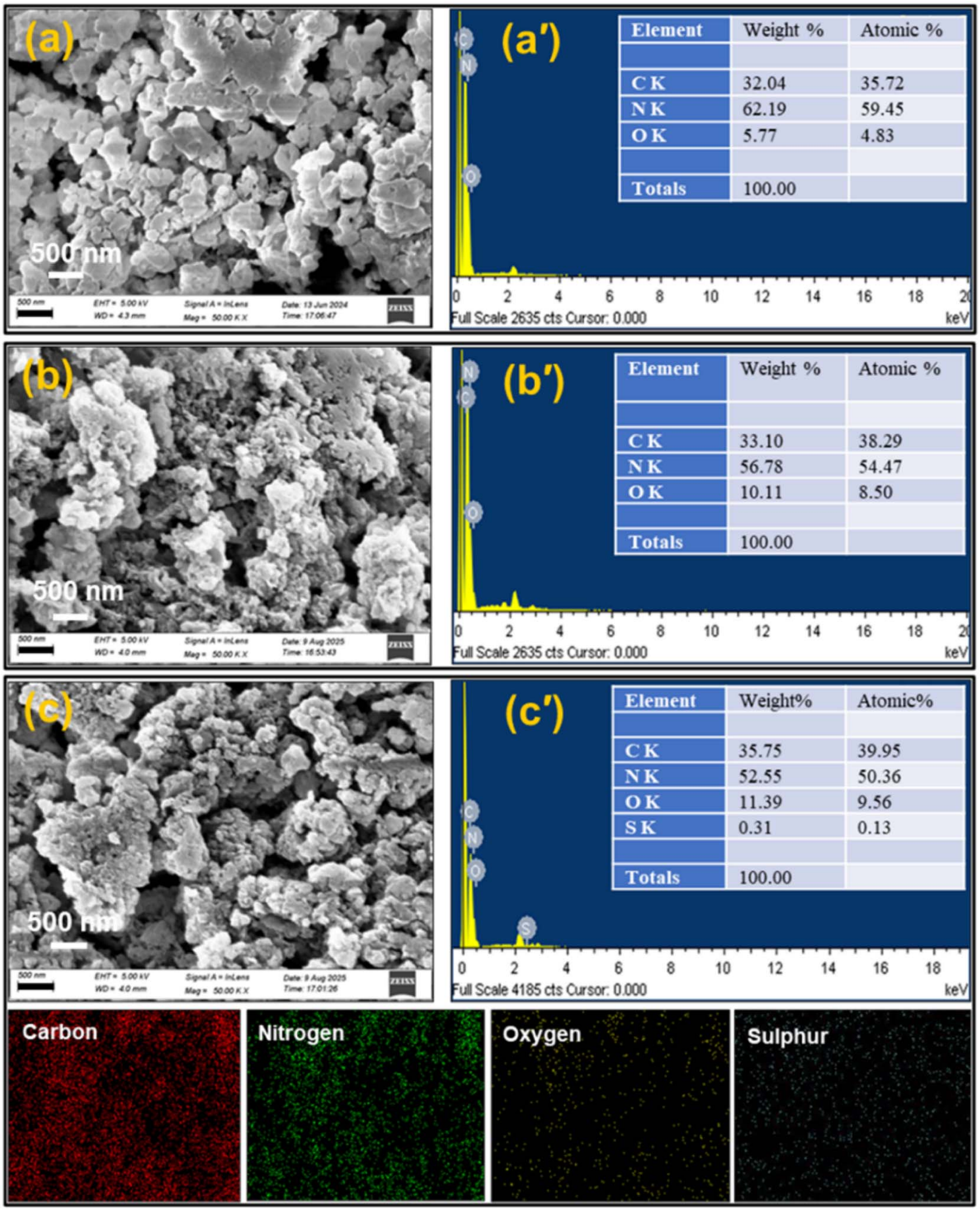

Element	Weight %	Atomic %
C K	32.04	35.72
N K	62.19	59.45
O K	5.77	4.83
Totals	100.00	

Element	Weight %	Atomic %
C K	33.10	38.29
N K	56.78	54.47
O K	10.11	8.50
Totals	100.00	

Element	Weight%	Atomic%
C K	35.75	39.95
N K	52.55	50.36
O K	11.39	9.56
S K	0.31	0.13
Totals	100.00	

Fig. 3 SEM micrographs of (a) pristine CN, (b) oxidized CN (Ox-CN), and (c) BSA-functionalized CN (BSA-CN) along with corresponding EDX spectra (a'–c') and elemental mapping images of all the constituent elements of BSA-CN.

ratio, provides direct evidence of protein attachment on the CN surface. These observations correlate strongly with the zeta potential results, where surface charge reversals (from −11.9 mV for CN to −23.3 mV for BSA-CN) confirmed successful stepwise functionalization. The elemental mapping images further validate the homogeneous distribution of carbon, nitrogen, oxygen, and sulphur across the BSA-CN surface. The uniform sulphur distribution is especially strong evidence of successful and consistent protein immobilization, confirming that BSA is not merely adsorbed in isolated patches but forms a uniform coating around the CN framework.

To further verify the nanoscale surface modifications induced by BSA functionalization and to complement the morphological features observed in SEM, TEM analysis was performed. As shown in Fig. S3 pristine CN exhibits stacked plate-like nanosheets with relatively smooth surfaces. The TEM micrographs of BSA-CN shown in Fig. 4 reveal aggregated, sheet-like domains with irregular edges, consistent with the layered morphology of graphitic carbon nitride. At lower magnification (Fig. 4(a), 200 nm scale), BSA-CN appears as loosely packed agglomerates of ultrathin flakes, indicating the presence of nanosheet-like structures. Increasing magnification

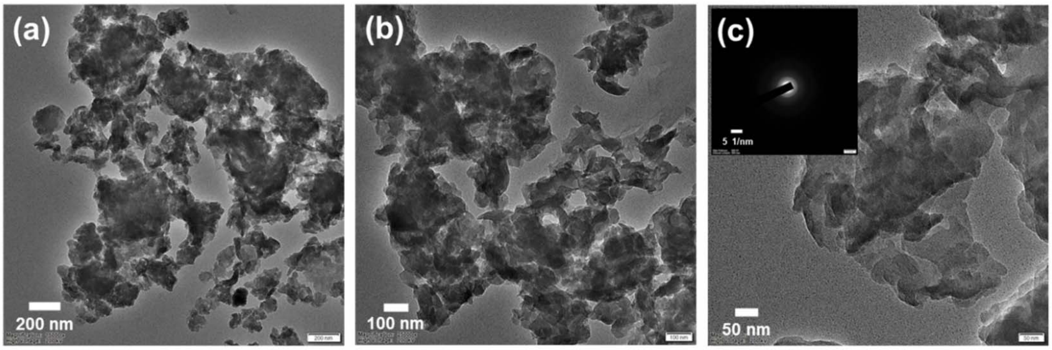

Fig. 4 TEM images of BSA-functionalized g-C_3N_4 (BSA-CN) at different magnifications: (a) 200 nm, (b) 100 nm and (c) HRTEM image with the inset showing the SAED pattern.

(Fig. 4(b)) highlights the crumpled and wrinkled surface textures, which can be ascribed to both the inherent layered nature of CN and the adsorption of BSA macromolecules, leading to increased surface roughness and partial aggregation. The HRTEM image reveals that the lattice fringes of CN become less distinct, and the material exhibits diffuse contrast rather than well-ordered crystalline planes, suggesting that BSA immobilization introduces a degree of surface amorphization and disrupts the stacking order of CN nanosheets. This interpretation is supported by the selected area electron diffraction (SAED) pattern (inset, Fig. 4(c)), which displays diffuse concentric rings instead of sharp diffraction spots, confirming the polycrystalline to semi-amorphous character of BSA-CN.

The nitrogen adsorption–desorption isotherms of pristine CN and BSA-CN are presented in Fig. 5. We recorded the N_2 adsorption–desorption isotherms of two samples possessing different nanoparticle sizes at 80 °C under a continuous nitrogen flow for 18 hours. Both materials exhibit a characteristic type-II isotherm with a pronounced H3-type hysteresis loop at higher relative pressures ($P/P_0 > 0.8$), which is typical of mesoporous structures originating from slit-shaped pores and irregular interparticle voids. This confirms that the fundamental mesoporous architecture of graphitic carbon nitride is retained even after protein immobilization.[54] Pristine CN shows a moderate adsorption volume at low relative pressures, indicating the presence of limited micropores, followed by a gradual increase in the mid-pressure region, which corresponds to capillary condensation within the mesoporous channels. In contrast, BSA-CN exhibits substantially higher nitrogen uptake over the entire pressure range. The enhanced adsorption at low P/P_0 suggests an increase in accessible surface area or pore exposure due to partial exfoliation or loosening of CN layers during BSA functionalization. The specific surface area *versus* pore radius for each sample is represented as a histogram in Fig. 5(b). We have obtained specific surface areas of 75.885 m^2 g^{-1} and 132.424 m^2 g^{-1} together with pore radii of 1.7 nm and 1.9 nm, respectively, for CN and BSA-CN samples. This enhancement is consistent with the morphological observations from TEM and SEM, where BSA deposition introduced surface roughness and disrupted the dense stacking of CN nanosheets. Such structural modifications create additional adsorption sites.

3.2. Adsorption performance of the BSA-CN composite

The influence of key operational parameters such as contact time, initial Pb^{2+} ion concentration, adsorbent dosage, and solution pH on Pb^{2+} adsorption performance of the BSA-CN composite was systematically investigated and the results are

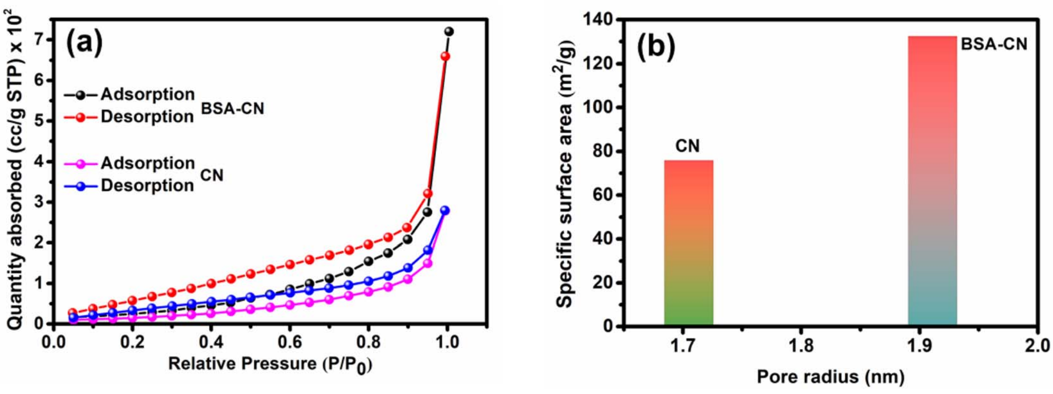

Fig. 5 (a) Nitrogen adsorption–desorption isotherms of pristine CN and BSA-CN, and (b) comparison of their BET specific surface areas and average pore radii.

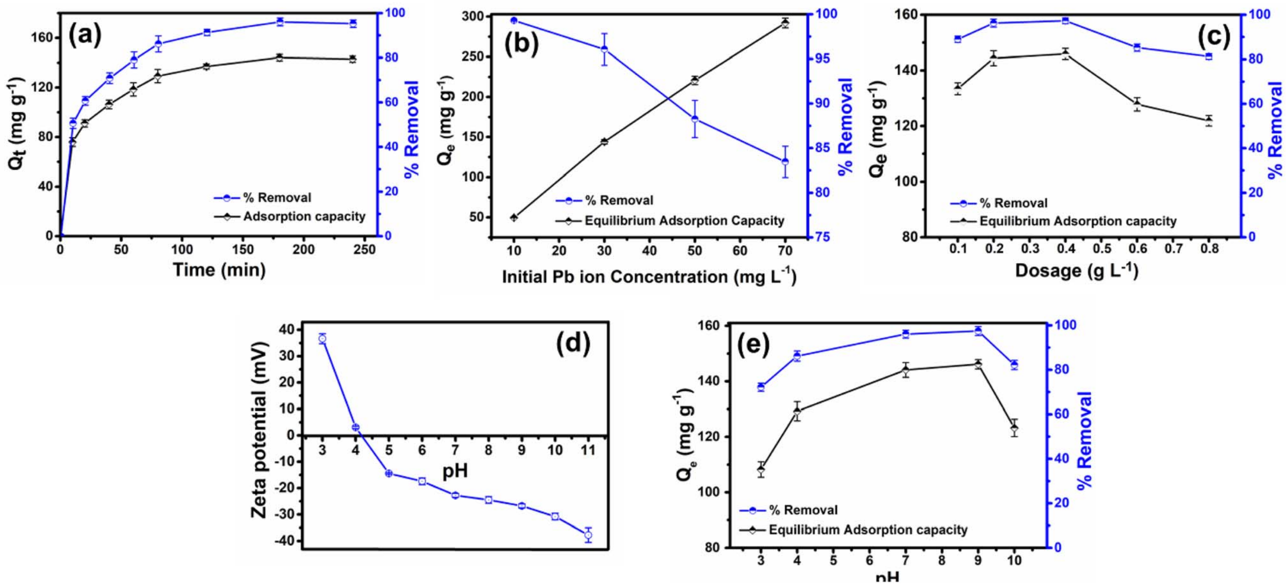

Fig. 6 (a) Effect of contact time, (b) initial Pb^{2+} concentration, (c) adsorbent dosage, (d) pH-dependent zeta potential of BSA-CN and (e) pH influence on equilibrium adsorption capacity and percentage removal of Pb^{2+} by adsorbent BSA-CN.

shown in Fig. 6. These variables significantly affect both equilibrium adsorption capacity (Q_t or Q_e) and percentage removal efficiency, and provide deep insight into the mechanistic aspects of metal uptake by the biofunctionalized nanosheets. Furthermore, to elucidate the impact of protein functionalization on adsorption efficiency, the Pb^{2+} adsorption performance of g-C_3N_4 (CN) was directly compared with that of BSA-CN under identical experimental conditions (Fig. S4 and Table S1). As shown, pristine CN shows a relatively low adsorption capacity of 59.8 mg g^{-1} at 30 ppm initial Pb^{2+} ion concentration due to the limited availability of strong metal-binding sites on its surface. In contrast, BSA-CN achieved a substantially enhanced adsorption capacity of 144.6 mg g^{-1}, corresponding to a 141.8% improvement relative to pristine CN. These substantial improvements confirmed that the introduction of multidentate protein derived functional groups, including carboxylate, amine and sulphur containing groups, enables strong surface complexation and cooperative chelation of Pb^{2+} ions.

3.2.1. Effect of contact time and initial Pb^{2+} concentration.

Fig. 6(a) shows the time-dependent adsorption profile of Pb^{2+} in terms of adsorption capacity and percentage removal. It was found that Pb^{2+} uptake was rapid during the initial 30–60 min, during which the adsorption capacity, Q_t increased sharply to approximately 119 mg g^{-1}. This initial fast phase can be attributed to the abundant availability of vacant adsorption or active sites, primarily surface amide, carboxyl, and nitrogen functionalities originating from immobilized BSA.[55] As the adsorption sites gradually became occupied, the adsorption rate gradually slowed and eventually reached at equilibrium around 150–180 min, where the maximum adsorption capacity approached ~145 mg g^{-1}. The corresponding Pb^{2+} removal efficiency exceeded 90%, highlighting the strong affinity of BSA-CN towards Pb^{2+} ions.

The influence of various initial Pb^{2+} concentrations (10, 30, 50 and 70 mg L^{-1}) was investigated to evaluate the initial aqueous solution concentration as illustrated in Fig. 6(b). It was revealed that the adsorption capacity increased steadily from 49.6 to nearly 292.1 mg g^{-1} as the initial Pb^{2+} concentration increased from 10 to 70 mg L^{-1}. Conversely, the removal efficiency declined from nearly 99.3% at 10 mg L^{-1} to 83.4% at 70 mg L^{-1}. This behavior could be ascribed to progressive saturation of available active sites and high concentration of adsorbate per unit mass of adsorbent.

3.2.2. Effect of adsorbent dosage.

The effect of adsorbent dosage was evaluated over the range of 0.1 to 0.8 g L^{-1} as shown in Fig. 6(c). It was observed that increasing the BSA-CN dosage from 0.1 to 0.4 g L^{-1} enhanced the removal efficiency from ~89% to 98%, indicating that a larger amount of BSA-CN provides more active sites for Pb^{2+} ions. However, the equilibrium adsorption capacity decreased from 145.9 to 121.8 mg g^{-1} with further increases in dosage. This decrease commonly reported in adsorption systems, arises from the potential aggregation of BSA-CN particles at higher loadings, which reduces the effective surface area and limits the accessibility of Pb^{2+} ions to inner binding sites.[56] Therefore, 0.2–0.4 g L^{-1} is identified as the effective dosage, balancing both adsorption efficiency and capacity.

3.2.3. Effect of solution pH.

According to previous studies, the surface chemistry of an adsorbent mainly depends on the pH of the solution.[47] Therefore, it is important to characterize the effect of solution pH in adsorption studies since the pH affects the availability of free sites if the metal binding groups are weakly basic or acidic. As shown in Fig. 6(d), the zeta potential of BSA-CN shows strong pH dependence, transitioning from +38 mV at pH 3 to −39 mV at pH 11. This sharp shift indicates that amine functionalities are positively charged under acidic pH conditions due to protonation and deprotonation of carboxyl and amide functionalities at higher pH leads to the development of a negative charge. The point of zero charge (pH_{pzc}) is observed near pH 4.2, after which the adsorbent becomes increasingly electronegative. This behavior is crucial for Pb^{2+} binding, as the metal ions interact strongly with negatively charged groups *via* electrostatic attraction and complexation.

The adsorption capacity as a function of pH (Fig. 6(e)) mirrors the zeta potential trend. Under strongly acidic conditions (pH 3), equilibrium adsorption capacity was relatively low (~118 mg g^{-1}), mainly due to the protonation of carboxylate and amine groups, which weakens their ability to coordinate with positively charge Pb^{2+}. In addition, high concentrations of H^+ ions competed directly with Pb^{2+} for the available adsorption sites.[57] With an increase in pH to 7–9, the equilibrium adsorption capacity of Pb^{2+} remarkably increased, raising Q_e to 158.2 mg g^{-1}. This improvement can be attributed to the deprotonation of carboxylate/amine groups and stronger coordination between Pb^{2+} and electron-rich donor sites in BSA ($-COO^-$, $-NH_2$, and $-C{=}O$). At pH 10, a decrease in Q_e is observed, which is likely due to the hydrolysis and precipitation of $Pb(OH)_2$, reducing the contribution of true adsorption. Thus, pH 6–8 represents the optimal range for BSA-CN and Pb^{2+} interactions.

3.3. Adsorption kinetics and isotherm

Adsorption kinetics provides crucial insights into the rate at which Pb^{2+} ions are adsorbed and the mechanisms that govern the overall adsorption process. Understanding these kinetic behaviors helps to identify whether the rate-limiting step involves surface reactions, diffusion, or chemical bonding. In this study, the adsorption kinetics of Pb^{2+} ions onto the synthesized BSA-CN composite were systematically investigated at 298 K with an initial Pb^{2+} concentration of 30 mg L^{-1} and an adsorbent mass of 0.2 g L^{-1}. To evaluate the adsorption kinetics, non-linear fitting of the pseudo first order (PFO), pseudo second order (PSO) and Elovich kinetic models as described in eqn (3)–(5), were used to fit the experimental data. The PFO model assumes that the rate of adsorption is directly proportional to the number of unoccupied sites. It generally represents a physisorption-driven process where mass transfer and surface diffusion dominate.[47] Conversely, PSO model assumes that chemisorption, involving electron sharing or exchange between the adsorbent and adsorbate, is the rate-controlling step.[58] Fig. 7(a) shows the fitting results of the three models and the corresponding parameters are summarized in Table 1.

The correlation coefficient (R^2), theoretical Q_e and reduced chi-square (χ^2-red) parameter values were used to assess model suitability. Among the three models, the Elovich model exhibited the best agreement with the experimental data when considering $R^2 = 0.994$ and a significantly lower value of χ^2-red (13.01), followed closely by the PSO model ($R^2 = 0.998$, χ^2-red = 27.66), whereas the PFO model showed a slightly lower correlation and χ^2-red ($R^2 = 0.941$, χ^2-red = 124.48). The PFO model yielded $Q_e = 135.61$ mg g^{-1} and $R^2 = 0.941$, underestimating the experimental value and suggesting that physisorption alone cannot adequately describe the system. Instead, the excellent fit of the PSO and Elovich models reflects the chemical nature and heterogeneity of the BSA-CN surface. The Q_e value predicted by the PSO model (148.42 mg g^{-1}) was closest to the experimental value. The PSO rate constant ($k_2 = 5.64 \times 10^{-4}$ g mg^{-1} min^{-1}) indicates that the adsorption process primarily follows a chemisorption mechanism, involving surface complexation or coordination between Pb^{2+} ions and the surface functional groups ($-COOH$, $-NH_2$, and $-C{=}O$) of the BSA-modified CN nanosheets.[59] The Elovich model fitting reveals notable correlations, characterized by best fit ($R^2 = 0.994$) a significantly higher adsorption rate constant ($\alpha = 62.1$ mg g^{-1} min^{-1}) compared to the desorption parameter ($\beta = 0.043$ g mg^{-1}), highlighting a strong adsorbent–adsorbate affinity and an energetically favorable adsorption process.[60] This disparity implies that Pb^{2+} ions interact robustly with diverse functional groups ($-COOH$, $-NH_2$, and amide) introduced through BSA immobilization, as evidenced by FTIR analyses, creating a variety of energetically distinct adsorption sites.

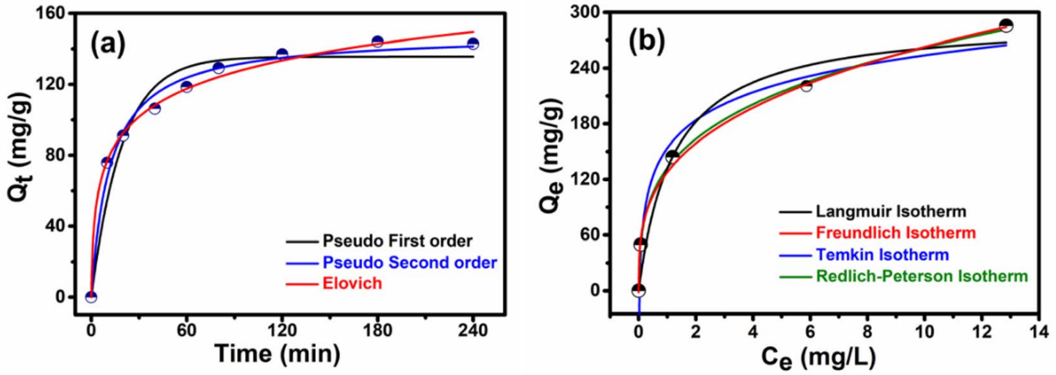

Fig. 7 (a) Nonlinear kinetic fitting of Pb^{2+} adsorption onto BSA-CN fitted with pseudo-first order, pseudo-second order, and Elovich models (T = 25 °C, C_o = 30 mg L^{-1}, m = 10 mg, V = 50 mL), (b) nonlinear isotherm fittings (Langmuir, Freundlich, Temkin, and Redlich–Peterson) for Pb^{2+} adsorption onto BSA-CN at 25 °C (t = 180 min, C_o = 30 mg L^{-1}, m = 10 mg, V = 50 mL).

Table 1 Kinetic parameters for the adsorption of Pb^{2+} ions onto BSA-CN ($T = 25$ °C, $C_o = 30$ mg L^{-1}, $m = 10$ mg, $V = 50$ mL)

Kinetic models	Parameters	Values
Pseudo first order	$Q_{e,\,exp}$ (mg g^{-1})	144.58
	Q_e (mg g^{-1})	135.61
	K_1 (min^{-1})	5.191×10^{-2}
	R^2	0.941
	χ^2 red	124.48
Pseudo second order	Q_e (mg g^{-1})	148.42
	K_1 (g mg^{-1} min^{-1})	5.64×10^{-4}
	R^2	0.988
	χ^2 red	27.66
Elovich kinetic model	α (mg g^{-1} min^{-1})	62.10
	β (g mg^{-1})	0.043
	R^2	0.994
	χ^2 red	13.01

In this work, equilibrium adsorption data for Pb^{2+} on the BSA-CN composite were fitted into different kinds of isotherm models (Langmuir, Freundlich, Temkin, and Redlich–Peterson) to examine the underlying adsorption process. All model fittings were performed using non-linear model fit to the original Q_e *vs.* C_e data as non-linear fitting minimizes residuals in the dependent variable (Q_e) directly and provides more reliable parameter estimates and uncertainty bounds than linearization.[61] The analysis of adsorption isotherms was conducted under controlled isothermal conditions of 298 K and a contact time of 180 min, sufficient to reach equilibrium. The adsorption isotherms and corresponding parameters of the Langmuir, Freundlich, Temkin and Redlich–Peterson models fitted to the experimental data are presented in Fig. 7(b) and Table 2 respectively. The fitting of the models was compared using both the coefficient of determination and reduced chi-square (χ^2_red) values to ensure rigorous statistical assessment.

Although all models showed reasonably good correlation ($R^2 > 0.95$), significant differences were observed in their error functions. The Redlich–Peterson model exhibited the highest R^2 (0.998) and the lowest χ^2 red value (24.34), confirming it as the most statistically appropriate descriptor of the adsorption system, followed closely by the Freundlich model as the superior descriptor of the data ($R^2 = 0.997$; χ^2 red = 40.54). Whereas Temkin ($R^2 = 0.977$; χ^2 red = 314.67) and Langmuir models ($R^2 = 0.953$; χ^2 red = 647.3) showed comparatively larger deviations from experimental data, thus statistically rejecting the foundational assumption of purely homogeneous, monolayer coverage described by the Langmuir model.[62] The R–P model, therefore, is designated as the optimal model for describing the equilibrium adsorption of Pb^{2+} onto the BSA composite. This statistical result is corroborated by the visual representation in Fig. 7(b), where the R–P isotherm and Freundlich isotherm curves overlay the experimental data points most accurately across the entire concentration range tested. The R–P model is advantageous because it incorporates characteristics of both the Langmuir model (when beta to 1) and the Freundlich model (when beta to 0). This hybrid nature allows it to accurately describe adsorption across a wide concentration range on both homogeneous and heterogeneous surfaces.[63] The critical parameter is the exponent β, which was determined to be 0.722. Since the value lies well within the favourable adsorption range ($0< \beta < 1$), this confirms that the adsorption process is decidedly non-ideal and occurs on a heterogeneous surface. The deviation of β from unity indicates that the BSA composite surface possesses multiple types of functional groups (*e.g.*, amino or carboxyl groups) with varying affinities for Pb^{2+} confirming a strong degree of heterogeneity in the binding sites. Furthermore, the strong affinity constant K_R (2934.6 L mg^{-1}) suggests that at lower concentrations, the binding is extremely favorable, indicative of specific, high-energy interactions. Further mechanistic validation was provided by the highly successful fit of the Freundlich isotherm, with parameters $K_F = 129.23$ and $n = 3.221$. This corresponds to a surface heterogeneity index $1/n$ of approximately 0.310. Since $1/n$ is well below 1, this result establishes the adsorption as highly favorable and confirms that the BSA-CN composite surface is heterogeneous, implying that the sorption energy exponentially decreases as the most energetic sites are progressively occupied.[64] Despite the inferior

Table 2 Adsorption isotherm parameter values for the adsorption of Pb^{2+} ions onto BSA-CN ($T = 25$ °C, $C_o = 30$ mg L^{-1}, $m = 10$ mg, $V = 50$ mL)

	Isotherm model	Model parameters	Values
1	Langmuir isotherm model	q_m (mg g^{-1})	292.94
		K_L (L mg^{-1})	0.821
		R^2	0.953
		χ^2 red	647.3
2	Freundlich isotherm model	K_F (mg g^{-1}) (L mg^{-1})$^{(1/n)}$	129.23
		n	3.221
		R^2	0.997
		χ^2 red	40.64
3	Temkin isotherm model	K_T (L mg^{-1})	35.59
		B	4.342×10^{-2}
		R^2	0.977
		χ^2 red	314.67
4	Redlich–Peterson isotherm model	K_R (L g^{-1})	2934.6
		a_R (L mg^{-1})$^{\beta}$	20.958
		β	0.722
		R^2	0.998
		χ^2 red	24.34

statistical fit, the Langmuir model provided the theoretical maximum monolayer capacity (Q_m) of 292.94 mg g^{-1}, confirming the synthesized material's high potential capacity for Pb^{2+} sequestration. Furthermore, the Temkin isotherm, with parameters $K_T = 35.59$ L mg^{-1} and $B = 4.342 \times 10^{-2}$, suggests that the heat of adsorption decreases linearly with increasing surface coverage, indicating significant adsorbate–adsorbate interactions or competitive site occupation typical of a strong physicochemical uptake mechanism. Collectively, the isotherm data robustly conclude that Pb^{2+} uptake onto the BSA composite is a favorable, complex, and mixed-mode physicochemical process dominated by surface heterogeneity, where multiple functional groups contribute to binding across the concentration range. The adsorption capabilities of several other absorbents are compared in Table S3.

3.4. Effect of temperature and adsorption thermodynamics

During the adsorption process, temperature has an important effect on adsorption because it affects the diffusion rate of ions in the solution. Therefore, temperature experiments were carried out at four different temperatures (298 K, 308 K, 318 K and 328 K) to analyze the influence of temperature on adsorption of Pb^{2+} ions. Fig. 8(a) illustrates the effect of temperature and contact time on adsorption capacity of Pb^{2+} by BSA-CN for 30 mg L^{-1} initial Pb^{2+} ion concentration with 0.2 mg g^{-1} adsorbent concentration. With an increase in temperature, different behaviour was shown by the adsorbent. As the temperature increased the adsorption capacity of BSA-CN initially increased up to 318 K and then decreased with the increase in temperature. Therefore, the adsorption process was initially endothermic and become exothermic beyond 328 K. This is consistent with the previously reported studies.[65] The adsorption is influenced by chemical adsorption. It has been reported in the literature that the chemisorption first increases since a greater number of adsorbate ions acquire sufficient energy to undergo chemisorption, which is provided by an increase in temperature. A further increase in temperature leads to breaking of bonds between the adsorbate and adsorbent, resulting in a decrease in adsorption capacity.

In addition, to examine the thermodynamic evaluation, the activation energy of the adsorption process was calculated by using the Arrhenius equation (eqn (12)) The Arrhenius plot of log k_2 *vs.* $1/T$ obtained by plotting the rate constant (k_2) from the pseudo-second-order kinetic equation against temperature (298 K, 308 K and 318 K) is illustrated in Fig. S5. The plot exhibited excellent linearity ($R = 0.997$), confirming the temperature-dependent nature of the rate-controlling step. From the slope and intercept of the Arrhenius plot, the activation energy (E_a) and pre-exponential factor (A) were determined to be 5.592 kJ mol^{-1} and 53.74, respectively. A relatively moderate E_a value obtained from the slope suggests that Pb^{2+} adsorption on BSA-CN occurs *via* a chemisorption-dominated mechanism involving coordination interactions between Pb^{2+} ions and amino, carboxyl, and carbonyl groups of the immobilized protein. The combined thermodynamic and kinetic findings collectively establish that the adsorption of Pb^{2+} onto BSA-CN is spontaneous, endothermic, and facilitated by energetically favorable coordination interactions.

In order to further examine the thermodynamic properties of the adsorption process, enthalpy (ΔH, kJ mol^{-1}), entropy (ΔS, kJ mol^{-1}), and Gibbs free energy (ΔG, kJ mol^{-1}) were studied in this experiment and they were calculated with the help of Gibbs and van't Hoff equations described in Section 2.7. The equilibrium thermodynamic constant (K_{ad}) calculated at each temperature was used to determine $\Delta G°$ according to eqn (11), and the consistently negative $\Delta G°$ values (Table 3) confirm that the adsorption of Pb^{2+} onto BSA-CN is spontaneous at all tested temperatures. The van't Hoff plot ($\ln K_{ad}$ *vs.* $1/T$) was constructed to determine the ΔH and ΔS from the slope and intercept of the linear fit based on eqn (10). As observed, the adsorption increases from 298 K to 318 K, indicating an endothermic behaviour. However, at 328 K, the thermodynamic equilibrium constant (K_{ad}) decreases sharply suggests temperature dependent adsorption behaviour, where increased thermal energy may weaken adsorbate–adsorbent interactions, leading to partial desorption.[65] Since the van't Hoff model assumes constant enthalpy over the temperature range and requires linear behaviour of $\ln K_{ad}$ *vs.* $1/T$, the thermodynamic

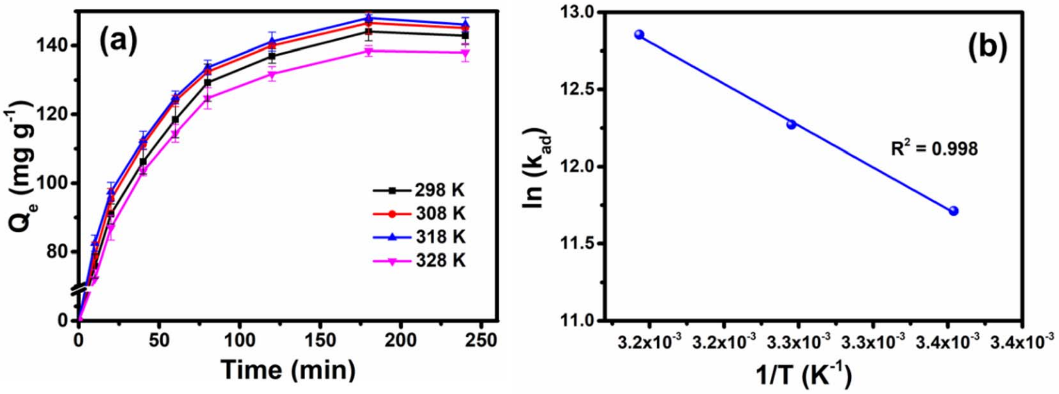

Fig. 8 Effect of temperature on Pb^{2+}adsorption by BSA-CN: (a) time-dependent adsorption capacity at different temperatures ($C_o = 30$ mg L^{-1}, $m = 10$ mg, $V = 50$ mL) and (b) van't Hoff plot ($\ln K_{ad}$ *versus* $1/T$) for the endothermic region (298–318 K).

Table 3 Thermodynamic parameters for adsorption of Pb^{2+} onto the BSA-BN composite. (C_o = 30 mg L^{-1}, m = 10 mg, V = 50 mL)

Temp. (K)	$\Delta G°$ (kJ mol^{-1})	$\Delta H°$ (kJ mol^{-1})	$\Delta S°$ (J mol^{-1} K^{-1})
298	−29.03	45.03	248.34
308	−31.44		
318	−34.00		
328	−30.02	—	—

parameters were calculated using the linear temperature region (endothermic region, 298–318 K) to ensure accuracy and reliability. The positive $\Delta H°$ value (45.03 kJ mol^{-1}) demonstrates that Pb^{2+} uptake is endothermic, which is consistent with increasing adsorption capacity at elevated temperatures. The high positive $\Delta S°$ value (248.34 J mol^{-1} K^{-1}) indicates increased randomness at the solid–liquid interface, likely due to the displacement of coordinated water molecules and structural relaxation of the protein matrix as Pb^{2+} ions bind to BSA functional groups.

3.5. Proposed adsorption mechanism of Pb^{2+} ions

The collective characterization results strongly support a multipathway, chemisorption-dominated adsorption mechanism for Pb^{2+} binding on BSA-CN. The initial rapid uptake observed within the first 30–50 min can be attributed to strong electrostatic attraction between Pb^{2+} ions and the negatively charged surface of BSA-CN (ζ = −23.3 mV), consistent with the pH-dependent surface charge behavior observed in zeta-potential measurements. FTIR and Raman spectra reveal the presence of amide I, II, and III, carboxylate ($-COO^-$), amine ($-NH_2$), and carbonyl (C=O) groups from BSA, along with pyridinic and graphitic nitrogen of $g\text{-}C_3N_4$. These oxygen and nitrogen-donor functionalities act as high-affinity coordination sites, enabling inner-sphere complexation of Pb^{2+} through multidentate chelation, which is consistent with the strong pseudo-second-order kinetic fit and the moderate activation energy (E_a = 5.592 kJ mol^{-1}) obtained from the Arrhenius analysis. The positive enthalpy change ($\Delta H°$ = +45.03 kJ mol^{-1}) further confirms the endothermic and chemically driven nature of Pb^{2+} binding, requiring energy to form stable coordination bonds with the protein-derived functional groups. Additionally, SEM, TEM and BET analyses show that BSA immobilization increases surface roughness, mesoporosity, and surface area, facilitating faster diffusion and providing a larger population of accessible binding sites. The Freundlich isotherm fit ($1/n < 1$) indicates heterogeneous sorption sites, implying that both high-energy BSA coordination pockets and lower-energy CN defects participate in Pb^{2+} uptake, while the high selectivity seen in multi-ion experiments confirms the strong preference of these sites for Pb^{2+} over other divalent cations. Therefore, the experimental results converge to support a mechanism in which Pb^{2+} adsorption proceeds through (i) electrostatic attraction, (ii) surface complexation with BSA functional groups and CN nitrogen centers, and (iii) diffusion into mesopores followed by heterogeneous site occupation. This integrated mechanism aligns with similar protein-modified adsorbent systems reported in the literature, and explains the superior adsorption performance, selectivity, and thermodynamic favorability observed for BSA-CN (Fig. 9).

3.6. Selectivity and reusability performance of BSA-CN

To evaluate the ion binding preference of the BSA-CN composite, competitive adsorption experiments were conducted using five environmentally relevant divalent metal ions Pb^{2+}, Cd^{2+}, Mn^{2+}, Zn^{2+} and Cu^{2+} at two different initial concentrations

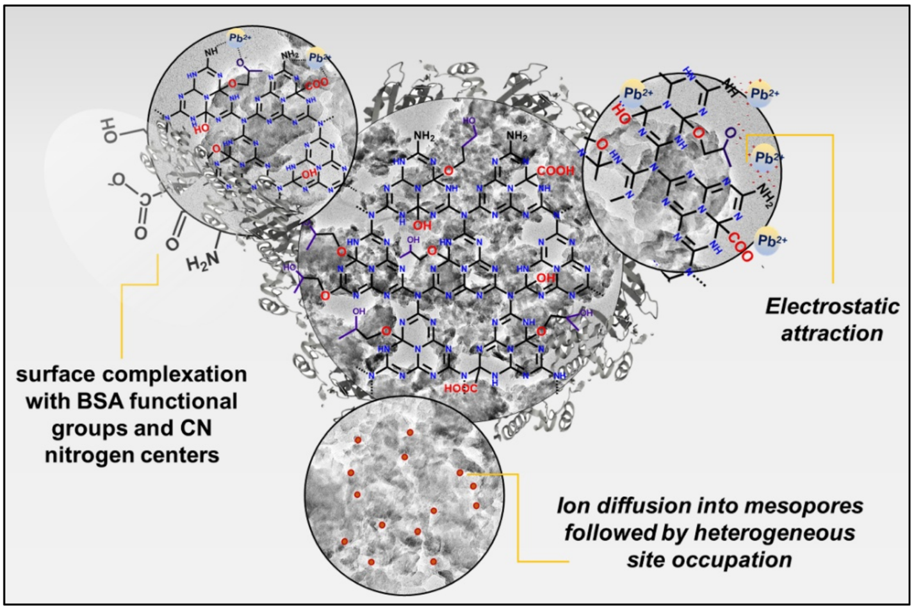

Fig. 9 Schematic illustration of the mechanisms of BSA-CN for Pb^{2+}.

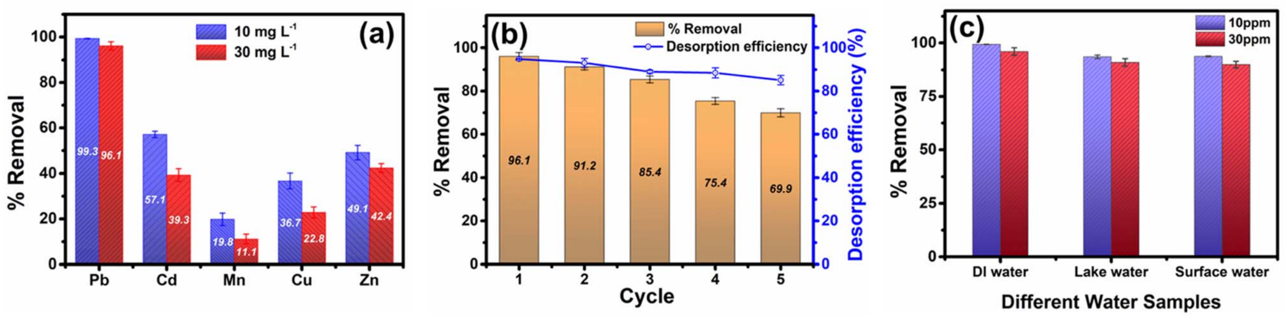

Fig. 10 (a) Comparative removal efficiencies of Pb^{2+}, Cd^{2+}, Mn^{2+}, Zn^{2+} and Cu^{2+} at 10 and 30 mg L^{-1} initial metal ion concentration, (b) reusability and desorption efficiency of BSA-CN over five adsorption–desorption cycles, and (c) comparison of Pb^{2+} removal efficiency of BSA-CN in deionized water and real water samples under identical adsorption conditions.

(10 and 30 mg L^{-1}). As shown in Fig. 10(a), BSA-CN displayed a pronounced selectivity toward Pb^{2+}, achieving removal efficiencies of 99.3% and 96.1% at 10 and 30 mg L^{-1}, respectively. In contrast, the removal of Cd^{2+}, Cu^{2+}, Zn^{2+} and Mn^{2+} was significantly lower, ranging from 39–57%, 22–37%, 42–49% and 11–19%, respectively. This superior affinity for Pb^{2+} can be attributed to the strong coordination interactions between Pb^{2+} ions and the protein-derived functional groups (–COO^-, –NH_2, –C=O, and sulfhydryl residues) present on the BSA-modified nanosheets. Pb^{2+} possesses high electronegativity, a large ionic radius, and a strong tendency to form inner-sphere complexes, which collectively enhance its binding affinity relative to other metal ions.[66] Furthermore, the immobilization of BSA introduces heterogeneous, high-density binding domains that resemble natural metal-binding sites in proteins, thereby enhancing selective complexation. The lower uptake of Cd^{2+}, Cu^{2+}, and Mn^{2+} suggests weaker interactions due to their differing ionic radii, hydration energies, and coordination preferences. These findings confirm that the BSA-CN composite is intrinsically selective toward Pb^{2+}, making it suitable for targeted remediation of lead-contaminated water.

Reusability and regeneration are critical parameters for any adsorbent that determine the practical and economic applicability. Therefore, reusability tests were performed for five consecutive adsorption–desorption cycles. For each cycle 20 mg of BSA-CN were added to 50 mL of Pb^{2+} solution with 180 rpm agitation at 25 °C for 180 min. Fig. 10(b) shows the percentage removal and desorption efficiency of Pb^{2+} from BSA-CN. In the first cycle the composite shows the highest percentage removal of 96.2% and a desorption efficiency of 94.9% under acidic conditions, causing the protonation of the adsorbent surface and allowing the desorption of positively charge Pb^{2+} ions from the adsorbent.[67] A gradual decline in performance was observed over successive cycles, with removal efficiencies decreasing to 91.2%, 85.4%, 75.4%, and 69.9% in cycles 2–5, respectively, while desorption efficiency values remained relatively high (85–95%) throughout the cycle. The slight decline in adsorption capacity is likely due to partial blockage, irreversible occupation of high-affinity sites or mild protein conformational changes during repeated washing and desorption processes. To verify the structural stability of the composite after mild acid (0.1 M HCl) treatment, FTIR and zeta potential analyses were conducted after cycle 1 and cycle 3, as illustrated in Fig. S7. The FTIR spectra retained the characteristic amide I band (~1632 cm^{-1}) and the weaker feature of N–H bending and C–N stretching at around 1544 cm^{-1} of BSA without significant peak shifts and disappearance, confirming the preservation of the protein backbone structure. Additionally, zeta potential measurements showed only minor variations in surface charge values to −20.3–21 mV compared to BSA-CN (−23.3 mV) in neutral medium, indicating that the immobilized BSA layer remained chemically stable and was not significantly leached during regeneration. The slight shifts may be due to the protonation/deprotonation effect during regeneration.

3.7. Pb^{2+} removal from real water samples

After a series of adsorption experiments, the practical applicability of the BSA-CN composite was evaluated using real environmental water samples collected from surface water influenced by industrial activities at Paschim Boragaon, Guwahati-35, Assam, India, and from Deepor Beel lake water, a Ramsar-designated wetland in Assam. Prior to analysis, the samples were filtered through a 0.45 μm membrane to remove suspended particulates and characterized for pH, conductivity and total dissolved solids to establish baseline water chemistry. As the native Pb^{2+} ion concentration was below the detection limit, we spiked the samples with known Pb^{2+} concentrations of 10 and 30 mg L^{-1} to simulate moderately and highly contaminated scenarios. Adsorption experiments were performed under similar conditions to those used for DI water solutions (pH 7.0, 0.2 g L^{-1} adsorbent dosage, 25 °C, 180 min). Under these conditions, BSA-CN exhibited a high Pb^{2+} removal efficiency of 89–90% in both collected real water matrices, retaining more than 90% of its adsorption capacity compared to deionized water (Table S2 and Fig. 10(c)). The slightly reduced Pb^{2+} ion adsorption capacity observed in real water samples can be attributed to the competitive adsorption from coexisting ions and dissolved species. These results confirm the robustness and selectivity of BSA-CN under realistic water chemistry conditions, highlighting its suitability for practical water treatment applications. The effectiveness observed corresponds with the recent literature reports on Pb^{2+} removal from real water systems. For

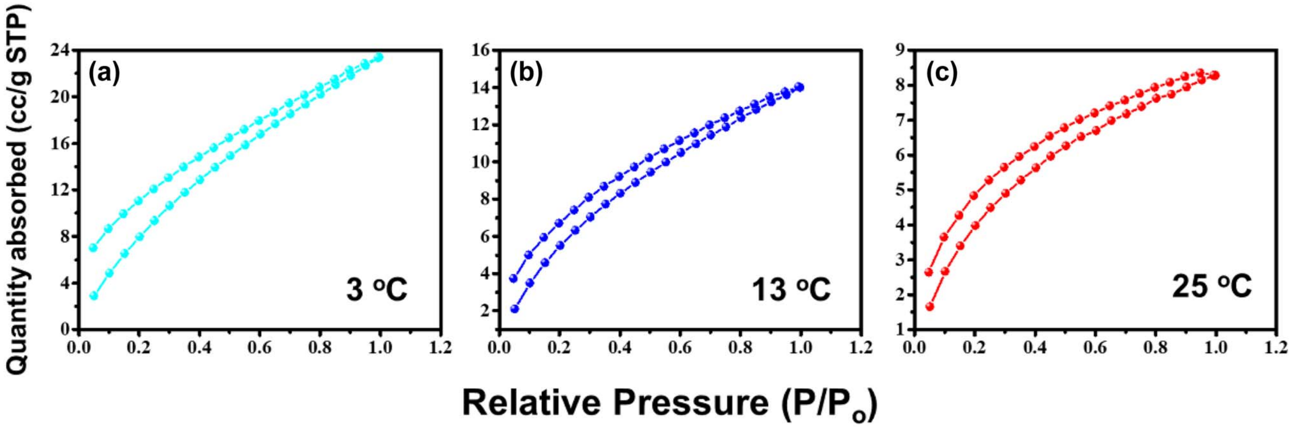

Fig. 11 CO_2 adsorption isotherms of BSA-CN at (a) 3 °C, (b) 13 °C, and (c) 25 °C respectively.

instance, Mamaghani *et al.* reported effective Pb^{2+} recovery from diverse environmental waters using a magnetic chitosan hydrogel adsorbent, highlighting the influence of competitive binding in complex matrices ($q_m \approx 31.7$ mg g^{-1}).[68] Similarly, a ZnO–biochar nanocomposite showed greater than 90% Pb^{2+} removal from wastewater, emphasizing the critical role of surface functionality and porosity in real-world applications. Moreover, comparative studies reveal that adsorption efficiencies in real wastewater are often slightly lower than those recorded in synthetic solutions due to competing divalent cations and dissolved organic matter.[69]

3.8. CO_2 adsorption, recyclability and mechanistic analysis

The CO_2 adsorption characteristics of the BSA-CN composite were investigated to assess its potential for low-pressure gas capture using a gas analyzer. CO_2 adsorption on the BSA-CN nanocomposite material was carried out at temperatures of approximately 25 °C, 13 °C, and 3 °C. As shown in Fig. 11(a–c), the CO_2 adsorption isotherms exhibit a gradual increase in uptake with increasing pressure, indicating favorable interactions between CO_2 molecules and the functionalized g-C_3N_4 surface. The BSA-CN nanocomposites demonstrated increasing adsorption capacities with decreasing temperature, reaching 8.35 cm^3 g^{-1} at 25 °C, 14.06 cm^3 g^{-1} at 13 °C and 23.44 cm^3 g^{-1} at 3 °C. The enhanced adsorption at lower temperatures can be attributed to the reduced kinetic energy of CO_2 molecules, which facilitates stronger adsorptive interactions with the surface.[70,71] After complete desorption, the retained CO_2 volumes were 2.65, 3.73, and 7.04 cm^3 g^{-1}. The observed CO_2 uptake is primarily associated with the presence of protein-derived functional groups, including amine (–NH_2), amide (–CONH–), and carboxylate (–COO^-) moieties, which introduce additional basic and polar sites capable of interacting with CO_2 through hydrogen bonding and weak acid–base interactions. Importantly, the BSA functionalization does not compromise the structural integrity of the g-C_3N_4 framework, allowing accessible adsorption sites without significant pore blockage. The N_2 BET analysis revealed that the porous structure formed by the particle arrangement favors the trapping of small molecules such as CO_2 (kinetic diameter ≈0.33 nm).[72] Additionally, following the desorption process, residual CO_2 volumes of 2.65, 3.73, and 7.04 cm^3 g^{-1} were recorded at 25 °C, 13 °C and 3 °C, respectively. This retained CO_2 is likely due to strong binding interactions between CO_2 molecules and chemically active sites, which hinder complete removal under standard desorption conditions.[73] Overall, the enhanced adsorption at lower temperatures contributes to increased CO_2 capture and residual retention after desorption, driven by stronger adsorptive interactions and confinement effects in the nanocomposite structure. A comparison with reported adsorbents (Table S4) indicates that BSA-CN exhibits adsorption performance comparable to or superior that of several biomass-derived carbons and inorganic nanocomposites.

The recyclability of CO_2 adsorption on the BSA–CN sample was evaluated at 3 °C, as shown in Fig. S8(a and b), yielding an adsorption capacity of 23.40 cm^3 g^{-1} in the second cycle. A minor decrease in CO_2 capture was observed during the second cycle; however, the adsorption capacity remained considerable. The retention value of 6.01 cm^3 g^{-1} suggests that the material possesses good recyclability for repeated CO_2 adsorption.

4. Conclusion

This study demonstrates a BSA protein functionalized strategy to transform g-C_3N_4 into a dual function adsorbent for selective Pb^{2+} removal and low-pressure CO_2 capture. The stepwise oxidation, epoxidation and amine coupling strategy enable stable covalent immobilization of BSA onto g-C_3N_4 nanosheets which introduces abundant amino, carboxyl and peptide binding domains, effectively enhancing the charge characteristics and adsorption capacity. Batch adsorption experiments revealed that BSA-CN demonstrates significant affinity for Pb^{2+} over a broad pH spectrum, with optimal absorption occurring under nearly neutral conditions. Kinetic assessments uncovered that the pseudo-second-order (PSO) model provided the optimal fit, highlighting that chemisorption is regulated by strong surface complexation. Isotherm modeling showed strong correlation with the Redlich–Peterson (R–P) model, followed closely by the Freundlich model, validating that Pb^{2+} adsorption onto BSA-CN occurs on a structurally heterogeneous surface with energetically diverse active sites introduced *via* BSA modification. The β parameter further confirms the mixed mechanism, reflecting the complex binding environment present on the biofunctionalized g-C_3N_4 nanosheets. The thermodynamic factors, including a negative $\Delta G°$, a positive $\Delta H°$, and $\Delta S°$, indicate that the adsorption phenomenon occurs spontaneously, with an endothermic nature and is driven by entropy, aligning well with the formation of metal–ligand complexes. The selectivity test indicates that BSA-CN shows a clear preference for Pb^{2+} ions, even with competing metal ions like Cd^{2+}, Cu^{2+}, Zn^{2+} and Mn^{2+} around, reaching a removal efficiency greater than 90% under favorable conditions. The material proved its capability to sustain a 70–90% level of adsorption efficiency throughout five regeneration cycles, underlining its impressive durability and reusability. In addition, the composite displayed low pressure CO_2 adsorption, with uptake increasing at lower temperatures due to strong interactions with protein derived functional groups and confinement effects within the nanocomposite structure. In essence, BSA-CN identifies itself as a remarkable, specifically targeted, and reusable bioengineered adsorbent. The synthesis of biological functionality with the resilient framework of carbon nitride establishes a promising foundation for innovative wastewater treatment methodologies and multifunctional environmental remediation strategies.

Conflicts of interest

The authors declare no conflict of interest.

Data availability

The raw data have been stored in IASST's D – space repository.

Supplementary information (SI): ZETA potential graph of g-C_3N_4, Ox-CN, Ep-CN and BSA-CN; AFM image and corresponding height profile of Ox-CN; TEM images of as synthesised g-C_3N_4 and SAED pattern; Pb^{2+} ion adsorption comparison of CN and BSA-CN; Arrhenius plot of log k_2 vs. $1/T$; SEM of BSA-CN after Pb^{2+} adsorption along with corresponding EDX spectra; FTIR spectra of BSA-CN after Pb^{2+} and CO_2 adsorption respectively; FTIR spectra of fresh BSA-CN and after the 1st and 3rd adsorption–desorption cycles and corresponding zeta potential distributions after cycle 1 and cycle 3; recyclability of CO_2 adsorption isotherm of BSA-CN at 276 K, equilibrium Pb^{2+} adsorption comparison of CN and BSA-CN; Pb^{2+} adsorption performance in real water samples; comparative analysis of Pb^{2+} adsorption capacity of BSA-CN with other materials; comparison of CO_2 adsorption capacity. See DOI: https://doi.org/10.1039/d5na01167a:.

Acknowledgements

BM and RS thank the UGC, New Delhi, for fellowships. The authors are grateful to IASST for in-house project support and research facilities and to SAIC-IASST Guwahati for instrumental facilities.

References

1 X. Y. D. Soo, J. J. C. Lee, W.-Y. Wu, L. Tao, C. Wang, Q. Zhu and J. Bu, Advancements in CO_2 capture by absorption and adsorption A comprehensive review, *J. CO_2 Util.*, 2024, **81**, 102727.

2 D. Piwowarska, E. Kiedrzyńska and K. Jaszczyszyn, A global perspective on the nature and fate of heavy metals polluting water ecosystems, and their impact and remediation, *Crit. Rev. Environ. Sci. Technol.*, 2024, **54**(19), 1436–1458.

3 A. Gonzalez-Villalva, R. L. Marcela, L.-V. Nelly, B.-N. Patricia, M. R. Guadalupe, C. T. Brenda, C. V. M. Eugenia, U. C. Martha, G. P. Isabel and T. I. Fortoul, Lead systemic toxicity A persistent problem for health, *Toxicology*, 2025, **515**, 154163.

4 R. Thakur, S. Singh, A. Chauhan, P. Kumar, R. V. Saini and A. K. Saini, Lead and arsenic toxicity, emerging mechanisms, immunotoxic effects, and future research perspectives, *BioMetals*, 2025, **38**, 1421.

5 N. Ihsanullah, A. Abbas, A. M. Al-Amer, T. Laoui, M. J. Al-Marri, M. S. Nasser, M. Khraisheh and M. A. Atieh, Heavy metal removal from aqueous solution by advanced carbon nanotubes Critical review of adsorption applications, *Sep. Purif. Technol.*, 2015, **157**, 141.

6 M. Filonchyk, M. P. Peterson, L. Zhang, V. Hurynovich and Y. He, Greenhouse gases emissions and global climate change Examining the influence of CO_2, CH_4, and N_2O, *Sci. Total Environ.*, 2024, **935**, 173359.

7 Z. Xu, S. Gu, D. Rana, T. Matsuura and C. Q. Lan, Chemical precipitation enabled UF and MF filtration for lead removal, *J. Water Process Eng.*, 2021, **41**, 101987.

8 V. K. Gupta, I. Ali, T. A. Saleh, A. Nayak and S. Agarwal, Chemical treatment technologies for waste-water recycling an overview, *RSC Adv.*, 2012, **2**, 6380.

9 A. I. Khdair, G. A. Aburumman, S. Gholipour and M. Afrand, Nanoparticles in water purification multifunctional roles, challenges, and sustainable applications, *Environ. Sci. Nano*, 2025, **12**, 3871.

10 X. Song, P. Li, Q. Shen, W. Wei and H. Yan, Study on the influence of different factors on the direct treatment of high turbidity water by microfiltration processes, *RSC Adv.*, 2025, **15**, 22699.

11 Z. Zheng, J. He, Z. Zhang, A. Kumar, M. Khan, C. W. Lung and I. M. C. Lo, Magnetically recyclable nanophotocatalysts in photocatalysis-involving processes for organic pollutant removal from wastewater current status and perspectives, *Environ. Sci. Nano*, 2024, **11**, 1784.

12 B. M. Larin and E. B. Yurchevskii, Problems of Ion-Exchange and membrane water treatment technologies in power engineering, *Therm. Eng.*, 2019, **66**, 744.

13 Z. Lin, X. Hu, H. Lin, G. Yu, L. Shen, W. Yu, B. Li, L. Zhao and M. Ying, Membrane technology for microplastic removal Microplastic occurrence, challenges, and innovations of process and materials, *Chem. Eng. J.*, 2025, **520**, 166183.

14 M. Priyadarshini, I. Das, M. M. Ghangrekar and L. Blaney, Advanced oxidation processes: Performance, advantages, and scale-up of emerging technologies, *J. Environ. Manage.*, 2022, **316**, 115295.

15 B. Wang, J. Lan, C. Bo, B. Gong and J. Ou, Adsorption of heavy metal onto biomass-derived activated carbon review, *RSC Adv.*, 2023, **13**, 4275.

16 K. H. H. Aziz, F. S. Mustafa, K. M. Omer, S. Hama, R. F. Hamarawf and K. O. Rahman, Heavy metal pollution in the aquatic environment efficient and low-cost removal approaches to eliminate their toxicity a review, *RSC Adv.*, 2023, **13**, 17595.

17 C. Das, S. Singh, S. Bhakta, P. Mishra and G. Biswas, Bio-modified magnetic nanoparticles with Terminalia arjuna bark extract for the removal of methylene blue and lead (II) from simulated wastewater, *Chemosphere*, 2021, **291**, 132673.

18 L. Pellenz, C. R. S. De Oliveira, A. H. Da Silva Júnior, A. H. Da Silva Júnior, L. J. S. Da Silva, L. Da Silva, A. A. U. De Souza, S. M. De Arruda Guelli Ulson De Souza, F. H. Borba, A. Da Silva and A. Da Silva, A comprehensive guide for characterization of adsorbent materials, *Sep. Purif. Technol.*, 2022, **305**, 122435.

19 D. Ewis, M. M. Ba-Abbad, A. Benamor and M. H. El-Naas, Adsorption of organic water pollutants by clays and clay minerals composites A comprehensive review, *Appl. Clay Sci.*, 2022, **229**, 106686.

20 X. Yang, Y. Zhou, J. Hu, Q. Zheng, Y. Zhao, G. Lv and L. Liao, Clay minerals and clay-based materials for heavy metals pollution control, *Sci. Total Environ.*, 2024, **954**, 176193.

21 M. Ahmad, A. U. Rajapaksha, J. E. Lim, M. Zhang, N. Bolan, D. Mohan, M. Vithanage, S. S. Lee and Y. S. Ok, Biochar as a sorbent for contaminant management in soil and water A review, *Chemosphere*, 2013, **99**, 19.

22 O. A. Oyewo and S. S. Makgato, Photocatalytic Reduction of Cr(VI) and Pb(II) with Biogenically Synthesized Copper Oxide Nanoparticles Using an Extract of the Myriophyllum spicatum Plant, *Multidiscip. Res.*, 2023, **6**, 564–578.

23 N. Renu and T. Sithole, A review on regeneration of adsorbent and recovery of metals Adsorbent disposal and regeneration mechanism, *S. Afr. J. Chem. Eng.*, 2024, **50**, 39.

24 W. Peng, H. Li, Y. Liu and S. Song, A review on heavy metal ions adsorption from water by graphene oxide and its composites, *J. Mol. Liq.*, 2017, **230**, 496–504.

25 L. Mei, M. Sun, R. Yang, Y. Zhang, Y. Zhang, Z. Zhang, L. Zheng, Y. Chen, Q. Zhang, J. Zhou, Y. Zhu, K. M. Y. Leung, W. Zhang, J. Fan, B. Huang, X. C. Zeng, H. S. Shin, C. Y. Tang, L. Gu, D. Voiry and Z. Zeng, Metallic 1T/1T′ phase TMD nanosheets with enhanced chemisorption sites for ultrahigh-efficiency lead removal, *Nat. Commun.*, 2024, **15**, 7770.

26 B. Mohan, U. Boruah, R. Sonkar, N. J. Mondal and D. Chowdhury, 2D-MOX 2 (X = S, SE, TE) and their Nanocomposite toward Sensing application: A review, *Part. Part. Syst. Charact.*, 2025, **42**, 2400156.

27 S. Essalmi, S. Lotfi, A. BaQais, M. Saadi, M. Arab and H. A. Ahsaine, Design and application of metal organic frameworks for heavy metals adsorption in water: a review, *RSC Adv.*, 2024, **14**, 9365–9390.

28 D. Bhanderi, P. Lakhani and C. K. Modi, Graphitic carbon nitride (g-C3N4) as an emerging photocatalyst for sustainable environmental applications a comprehensive review, *RSC Sustainability*, 2023, **2**, 265.

29 S. Soyer-Uzun, P. Yu, F. K. Öner and S. Sen, Mechanistic Understanding of Superior Methylene Blue Adsorption Capacity in a Novel g-C_3N_4 Modified Amorphous Na–Ca–Mg Silicate Adsorbent Insights from Multinuclear Solid-State NMR Spectroscopy, *J. Phys. Chem. B*, 2024, **128**, 12638.

30 M. A. Zorgani, F. Zaoui, R. N. E. H. Zorgani, B. E. Daouadji, F. Z. Sebba, E. Choukchou-Braham, B. Bounaceur, Y. Ma, M. Bhardwaj and H. Ma, Ultrasonic-assisted adsorption of heavy copper and lead metal ions by g-C3N4, application of g-C_3N_4@MNPs (M Pb, Cu) in the catalytic photoreduction of organic pollutants, *J. Water Process Eng.*, 2024, **58**, 104724.

31 D. C. Onwudiwe, N. Gobile, O. A. Oyewo and S. S. Makgato, Photocatalytic reduction of hexavalent chromium using Zn_2SnO_4–ZnO modified g-C_3N_4 composite, *Results Eng.*, 2023, **20**, 101521.

32 M. Kumari, N. Kumar, R. K. Sharma, S. Makgato, M. Tahir, Jogender and A. Kumari, Structural, computational, and electrochemical analysis of SnS_2 embedded g-C_3N_4/In_2O_3 heterostructures for photocatalytic decontamination of water pollutants, *Mater. Sci. Semicond. Process.*, 2025, **197**, 109658.

33 T. Muhmood, I. Ahmad, Z. Haider, S. K. Haider, N. Shahzadi, A. Aftab, S. Ahmed and F. Ahmad, Graphene-like graphitic carbon nitride (g-C3N4) as a semiconductor photocatalyst: Properties, classification, and defects engineering approaches, *Mater. Today Sustainability*, 2023, **25**, 100633.

34 X. Xu, Y. Xu, Y. Liang, H. Long, D. Chen, H. Hu and J. Z. Ou, Vacancy-modified g-C_3N_4 and its photocatalytic applications, *Mater. Chem. Front.*, 2022, **6**, 3143.

35 M. Majdoub, Z. Anfar and A. Amedlous, Emerging chemical functionalization of g-C_3N_4 Covalent/Noncovalent modifications and Applications, *ACS Nano*, 2020, **14**, 12390.

36 U. Boruah, B. Mohan, N. D. Choudhury and D. Chowdhury, Surface-Modified graphitic carbon nitride as a lubricant additive in Bio-Based oil, *ACS Appl. Nano Mater.*, 2025, **8**, 5430.

37 C. Zhang, J. Liu, X. Liu and S. Xu, D–π–A-type triphenylamine dye covalent-functionalized g-C_3N_4 for highly efficient photocatalytic hydrogen evolution, *Catal. Sci. Technol.*, 2020, **10**, 1609.

38 Y. Guo, S. Chu, S. Yan, Y. Wang and Z. Zou, Developing a polymeric semiconductor photocatalyst with visible light response, *Chem. Commun.*, 2010, **46**, 7325.

39 Q. Wang, S. Zhu, C. Xi and F. Zhang, A review Adsorption and Removal of Heavy metals based on Polyamide-amines composites, *Front. Chem.*, 2022, **10**, 814643.

40 H. A. Alhazmi, M. S. Alam, M. Albratty, A. Najmi, A. A. Abdulhaq, R. Hassani, W. Ahsan and A. N. Qramish, Binding Investigation of Some Important Metal Ions Copper (I), Nickel (II), and Aluminium (III) with Bovine

Serum Albumin Using Valid Spectroscopic Techniques, *J. Chem.*, 2023, **2023**, 1.

41 B. Boro, B. Mohan, M. Barman, P. Talukdar, A. Bala and D. Chowdhury, Chitosan–Collagen/h-BN nanocomposites: A sustainable approach to thermoelectric material design, *Mater. Sci. Eng., B*, 2026, **327**, 119255.

42 Y. Luo, Y. Zhang, Z. Xiong, X. Chen, A. Sha, W. Xiao, L. Peng, L. Zou, J. Han and Q. Li, Peptides used for heavy metal Remediation A promising approach, *Int. J. Mol. Sci.*, 2024, **25**, 6717.

43 H. A. Alhazmi, FT-IR Spectroscopy for the Identification of Binding Sites and Measurements of the Binding Interactions of Important Metal Ions with Bovine Serum Albumin, *Sci. Pharm.*, 2019, **87**, 5.

44 N. U. Amin, H. M. Siddiqi, Y. K. Lin, Z. Hussain and N. Majeed, Bovine Serum Albumin Protein-Based Liquid Crystal biosensors for optical detection of toxic heavy metals in water, *Sensors*, 2020, **20**, 298.

45 X. Yu, S. Sun, L. Zhou, Z. Miao, X. Zhang, Z. Su and G. Wei, Removing Metal Ions from Water with Graphene–Bovine Serum Albumin Hybrid Membrane, *Nanomaterials*, 2019, **9**, 276.

46 H. Mitsuda, F. Kawa, A. Yamamoto and K. Nakajima, Carbon dioxide-protein interaction in a gas-solid phase, *J. Nutr. Sci. Vitaminol.*, 1975, **21**, 151.

47 Md. Imtiaz-Ul-Islam, L. Hong and T. Langrish, CO_2 capture using whey protein isolate, *Chem. Eng. J.*, 2011, **171**, 1069.

48 K. K. Kriti, G. S. Chauhan, S. Chauhan and S. Sharma, Epichlorohydrin/triethylamine modified psyllium as a highly efficient adsorbent for selective adsorption of anionic dyes, *Int. J. Biol. Macromol.*, 2024, **294**, 139386.

49 J. Yang, X. Zhang, C. Xie, J. Long, Y. Wang, L. Wei and X. Yang, Preparation of g-C_3N_4 with High Specific Surface Area and Photocatalytic Stability, *J. Electron. Mater.*, 2021, **50**, 1067.

50 S. Pandit, S. Kundu and V. K. Aswal, Interaction among bovine serum albumin (BSA) molecules in the presence of anions a small-angle neutron scattering study, *J. Biol. Phys.*, 2022, **48**, 237.

51 Q. Yu, Q. Xu, H. Li, K. Yang and X. Li, Effects of heat treatment on the structure and photocatalytic activity of polymer carbon nitride, *Mater. Sci.*, 2019, **54**, 14599.

52 H. Li, Y. Jing, X. Ma, T. Liu, L. Yang, B. Liu, S. Yin, Y. Wei and Y. Wang, Construction of a well-dispersed Ag/graphene-like g-C_3N_4 photocatalyst and enhanced visible light photocatalytic activity, *RSC Adv.*, 2017, **7**, 8688.

53 N. Kuhar, S. Sil and S. Umapathy, Potential of Raman spectroscopic techniques to study proteins, *Spectrochim. Acta, Part A*, 2021, **258**, 119712.

54 G. Xin, Y. Xia, Y. Lv, L. Liu and B. Yu, Investigation of mesoporous graphitic carbon nitride as the adsorbent to remove Ni (II) ions, *Water Environ. Res.*, 2015, **88**, 318.

55 W. Lu, X. Liang, J. Liu, F. Jing, M. Jin, X. He, T. Wang and R. Yu, Mechanistic insights into heavy metal ion adsorption by 3-aminophenol-formaldehyde polymer adsorbents, *J. Ind. Eng. Chem.*, 2025, **153**, 572–583.

56 P. Thamarai, S. Karishma, V. C. Deivayanai, A. Saravanan and P. R. Yaashikaa, Theoretical and experimental analysis of Pb (II) ion adsorption using surface modified macroalgal biosorbents modelling and desorption study, *Ind. Eng. Chem. Res.*, 2024, **63**, 21505.

57 U. Haseen, S. Kapoor, R. A. Khan, H. Ahmad and B. H. Koo, In Situ Fabrication and Characterization of g-C3N4 onto Cellulose Nanofibers and Selective Separation of Heavy Metal Ions, *ACS Omega*, 2023, **9**, 1620.

58 E. D. Revellame, D. L. Fortela, W. Sharp, R. Hernandez and M. E. Zappi, Adsorption kinetic modeling using pseudo-first order and pseudo-second order rate laws A review, *Cleaner Eng. Technol.*, 2020, **1**, 100032.

59 Z. Liu, Q. Wang, X. Huang and X. Qian, Surface Functionalization of Graphene Oxide with Hyperbranched Polyamide-Amine and Microcrystalline Cellulose for Efficient Adsorption of Heavy Metal Ions, *ACS Omega*, 2022, **7**, 10944.

60 L. Largitte and R. Pasquier, A review of the kinetics adsorption models and their application to the adsorption of lead by an activated carbon, *Process Saf. Environ. Prot.*, 2016, **109**, 495.

61 B. Boulinguiez, P. L. Cloirec and D. Wolbert, Revisiting the Determination of Langmuir Parameters—Application to Tetrahydrothiophene Adsorption onto Activated Carbon, *Langmuir*, 2008, **24**, 6420.

62 J. N. Putro, S. P. Santoso, S. Ismadji and Y.-H. Ju, Investigation of heavy metal adsorption in binary system by nanocrystalline cellulose – Bentonite nanocomposite Improvement on extended Langmuir isotherm model, *Microporous Mesoporous Mater.*, 2017, **246**, 166.

63 J. Wang and X. Guo, Adsorption isotherm models Classification, physical meaning, application and solving method, *Chemosphere*, 2020, **258**, 127279.

64 K. Y. Foo and B. H. Hameed, Insights into the modeling of adsorption isotherm systems, *Chem. Eng. J.*, 2009, **156**, 2.

65 R. S. Bangari, A. K. Singh, S. Namsani, J. K. Singh and N. Sinha, Magnetite-Coated Boron Nitride Nanosheets for the Removal of Arsenic(V) from Water, *ACS Appl. Mater. Interfaces*, 2019, **11**, 19017.

66 B.-L. Zhang, W. Qiu, P.-P. Wang, Y.-L. Liu, J. Zou, L. Wang and J. Ma, Mechanism study about the adsorption of Pb(II) and Cd(II) with iron-trimesic metal-organic frameworks, *Chem. Eng. J.*, 2019, **385**, 123507.

67 V. K. Gupta, S. Agarwal and T. A. Saleh, Synthesis and characterization of alumina-coated carbon nanotubes and their application for lead removal, *J. Hazard. Mater.*, 2010, **185**, 17.

68 A. S. Mamaghani, M. Manafi and M. Hojjati, Pb $^{2+}$ recovery from real water samples by adsorption onto nano Fe $_3$ O $_4$/chitosan-acrylamide hydrogel ions in real water samples, *IET Nanobiotechnol.*, 2023, **17**, 337–351.

69 H. Mudassar, K. Hina, U. Ghani, Q. Afzaal, A. A. Shah, S. Shaffique and H. O. Elansary, Adsorptive removal of Pb^{2+} from wastewater using ZnO-Biochar nanocomposite, *Sci. Rep.*, 2025, **15**, 29517.

70 Z. Khoshraftar, A. Ghaemi and A. Hemmati, Comprehensive investigation of isotherm, RSM, and ANN modeling of CO_2 capture by multi-walled carbon nanotube, *Sci. Rep.*, 2024, **14**, 5130.

71 T. A. Saleh, Nanomaterials and hybrid nanocomposites for CO_2 capture and utilization environmental and energy sustainability, *RSC Adv.*, 2022, **12**, 23869.

72 S. Kumar, P. Puzari and S. Kundu, Phyllosilicate Clay Blended with Semiconductor Nanocomposite for Enhanced Dye Removal and CO_2 Adsorption, *ACS Appl. Nano Mater.*, 2025, **8**, 19283.

73 D. Kichukova, T. Lazarova, G. Atanasova, D. Kovacheva and I. Spassova, Tailored carbon nanocomposites for efficient CO_2 capture, *Molecules*, 2025, **30**, 2408.